Anisotropic contributions to the transferred hyperfine field in magnetic Sn compounds

Laura Katherine Perry
Department of Physics
McGill University
Montreal, Québec
CANADA

February 2006

A thesis submitted to
McGill University in partial
fulfillment of the requirements
for the degree of Master of Science

Library and
Archives Canada

Published Heritage
Branch

395 Wellington Street
Ottawa ON K1A 0N4
Canada

Bibliothèque et
Archives Canada

Direction du
Patrimoine de l'édition

395, rue Wellington
Ottawa ON K1A 0N4
Canada

Your file   Votre référence
ISBN: 978-0-494-24768-6
Our file   Notre référence
ISBN: 978-0-494-24768-6

NOTICE:
The author has granted a non-exclusive license allowing Library and Archives Canada to reproduce, publish, archive, preserve, conserve, communicate to the public by telecommunication or on the Internet, loan, distribute and sell theses worldwide, for commercial or non-commercial purposes, in microform, paper, electronic and/or any other formats.

The author retains copyright ownership and moral rights in this thesis. Neither the thesis nor substantial extracts from it may be printed or otherwise reproduced without the author's permission.

AVIS:
L'auteur a accordé une licence non exclusive permettant à la Bibliothèque et Archives Canada de reproduire, publier, archiver, sauvegarder, conserver, transmettre au public par télécommunication ou par l'Internet, prêter, distribuer et vendre des thèses partout dans le monde, à des fins commerciales ou autres, sur support microforme, papier, électronique et/ou autres formats.

L'auteur conserve la propriété du droit d'auteur et des droits moraux qui protège cette thèse. Ni la thèse ni des extraits substantiels de celle-ci ne doivent être imprimés ou autrement reproduits sans son autorisation.

In compliance with the Canadian Privacy Act some supporting forms may have been removed from this thesis.

While these forms may be included in the document page count, their removal does not represent any loss of content from the thesis.

Conformément à la loi canadienne sur la protection de la vie privée, quelques formulaires secondaires ont été enlevés de cette thèse.

Bien que ces formulaires aient inclus dans la pagination, il n'y aura aucun contenu manquant.

Canada

Abstract

The $RMn_6T_{6-x}X_x$ family of compounds (R = rare earth; T = Ge, Sn; X = Ga, In) has seen a lasting and intensive series of studies over the past several years. In these systems, a spin reorientation process, which is a pure rotation of the magnetic structure relative to the crystal axes, can be used to determine the anisotropic contributions to the transferred hyperfine fields at the Sn sites. The anisotropic contribution has been shown to be substantial in the $MnSn_2$ and $FeSn_2$ compounds, and is an important fraction of the overall transferred hyperfine field. A spin reorientation transition can be either temperature-induced, or field-induced (spin-flop). The temperature-induced spin reorientation generally results from a competition between the magnetocrystalline anisotropies of the rare earth and Mn sublattices. The substitution of Sn with Ga strongly affects the anisotropy, shown here to decrease the spin reorientation temperature with increasing x by 255 ± 18 K/Ga in $TbMn_6Sn_{6-x}Ga_x$. However, the sublattice anisotropies seem unaffected by In substitution, and the spin reorientation temperature is nearly constant throughout a large range of In concentration. A field-induced spin-flop can be achieved by applying a large enough field perpendicular to the direction of the moments.

In this study, we show how both the temperature-induced SR and field-induced SF allow for the anisotropic field to be isolated from the isotropic contribution. The consistency between the two measurements of the anisotropic field indicates that the magnitude of the anisotropic contribution is independent of the driving force of the reorientation. We show that a complete 90° spin reorientation occurs in the $ErMn_6Sn_{5.89}Ga_{0.11}$ and $TbMn_6Sn_{6-x}Ga_x$ compounds ($0.2 \leq x \leq 0.8$), as well as in $TbMn_6Sn_{5.46}In_{0.54}$ at room temperature for an applied field of 0.57(3) T. The site preference for Ga substitution is investigated and compared with former results. Finally, the anisotropic contribution at one of the Sn sites is shown to exceed 40% in all of the compounds investigated, and this site assignment is confirmed.

Résumé

La famille de composés $RMn_6T_{6-x}X_x$ (R = terre rare ; T = Ge, Sn ; X = Ga, In) a fait l'objet d'étude intense au cours des dernières années. Dans ces systèmes, un procédé de réorientation des moments magnétiques (une rotation pure de la structure magnétique relative aux axes crystallographiques) peut être utilisé pour déterminer les contributions anisotropes aux champs magnétiques hyperfins transférés aux sites de Sn, B_{hf}. La contribution anisotrope est grande dans les systèmes de $MnSn_2$ et de $FeSn_2$, et constitue une fraction importante du B_{hf} total. On induit une réorientation des moments magnétiques en changeant la température ou en appliquant un champ magnétique externe. En général, la réorientation *température-persuadée* est le résultat d'une compétition entre l'anisotropie magnétocrystalline de la terre rare et celle du Mn. Le remplacement du Sn par le Ga affecte fortement l'anisotropie, et une augmentation en x diminue la température de la transition (T_{sr}) par 255 ± 18 K/Ga dans $TbMn_6Sn_{6-x}Ga_x$. Cependant, l'anisotropie ne semble pas être affectée par le remplacement du Sn par l'In, et T_{sr} est presque constante au cours d'une série de concentrations d'In. Une réorientation *champ-persuadée* est induite en appliquant un grand champ magnétique perpendiculaire à la direction des moments magnétiques.

Dans cette étude, nous démontrons que la contribution anisotrope à B_{hf} peut être déterminée à l'aide des deux procédés de réorientation. Le fait que les deux mesures du champ anisotrope sont concordantes indique que l'ampleur de la contribution anisotrope ne dépend pas de la force d'entraînement qui induit la réorientation. Nous démontrons que, en conséquence d'une réorientation T-persuadé, les moments magnétiques subissent une rotation entière de 90° dans $RMn_6Sn_{6-x}Ga_x$ (R = Tb, Er; $0{,}2 \leq x \leq 0{,}8$), et aussi dans $TbMn_6Sn_{5.46}In_{0.54}$ à 300 K pour un champ magnétique externe de 0.57(3) T. Nous examinons aussi quel site de Sn subit la plus importante substitution avec le Ga, et le compare aux résultats obtenus par d'autres études. La contribution anisotrope à un des sites de Sn dépasse 40% dans tous les composés examinés, et l'identification de ce site est confirmé.

Acknowledgments

I wish to thank Leo Nikkinen, for teaching me to respect the conservation of functioning equipment, Robert Gagnon and John Smeros for showing me how to execute it, Gérard Venturini and Sean Cadogan, for having an extensive answer to my many many vague questions. I also wish to show my gratitude to Mark Orchard Webb and Christian Voyer, who have unlimited patience with me, and whose support, friendship and wisdom I value immensely. Thanks to my mom and dad because they're so good at loving me, to Dominic, for providing the inspiration and confidence to write this and understand it, and to Christian Bernard Roy, for being at my side, all the time.

Contents

List of Figures

List of Tables

Chapter 1

Introduction

1.1 Transferred hyperfine fields in Sn alloys

At a non-magnetic Mössbauer probe site in a crystal structure, any hyperfine field B_{hf} present at the site must be transferred to the atom from neighbouring magnetic moments. This form of hyperfine field is know as a *transferred hyperfine field*, and in a metallic system it receives two main contributions [1]: isotropic and anisotropic. As s electrons possess a non-vanishing probability inside the nuclear volume, they can interact directly with the nuclear moment [2]. The polarization of conduction electrons induces a spin imbalance at the nucleus, generating what is known as the Fermi contact field. This field is the isotropic contribution to B_{hf}, and it depends only on the magnitude of the neighbouring moments and the symmetry of their magnetic structure. The anisotropic contribution involves the bonding between the magnetic ion (typically a $3d$ transition metal such as Mn or Fe) and the non-magnetic Mössbauer probe, leading to a transferred field which depends on the relative orientations of the moments and their connecting bonds. The total transferred hyperfine field is given by [3]:

$$\mathbf{B}_{hf} = \left(\mathrm{A}_p \sum_{i=1}^{n} \mathbf{u}_i (\vec{\mu}_i \cdot \mathbf{u}_i) - \frac{\mathrm{A}_p}{3} \sum_{i=1}^{n} \vec{\mu}_i \right) + \mathrm{A}_s \sum_{i=1}^{n} \vec{\mu}_i \tag{1.1}$$

Compound	Site	B_{hf}^{meas} (T)	Nature of B_{hf}
$MnSn_2$	Sn_{00}	4.9(2)	Anisotropic
	Sn_{--}	6.9(2)	Iso + Aniso
	Sn_{+-}	10.3(2)	Iso + Aniso
	Sn_{++}	21.2(2)	Iso + Aniso
$FeSn_2$	All	2.7(2)	Anisotropic

Table 1.1: Measured hyperfine fields in $MnSn_2$ and $FeSn_2$ at 4.2 K. Sn_{00} in $MnSn_2$ is the only site for which the field is totally anisotropic, and comparing this anisotropic field to the total B_{hf} at the three other sites (which receive both isotropic and anisotropic contributions) demonstrates the significance of the anisotropic contribution. Results from [3].

where $\mathbf{u}_i$ is the unit vector connecting each Mössbauer probe to a $3d$ neighbour (there are n of them) with moment $\vec{\mu}_i$. A_p and A_s are the dipolar (anisotropic) and contact (isotropic) fields due to a unit $3d$ moment. The first two terms represent the anisotropic contribution to B_{hf}, while the last term is the isotropic contribution.

In the tetragonal $CuAl_2$-type $MnSn_2$ and $FeSn_2$ stannides, the Sn atoms are the non-magnetic Mössbauer probes, and the $3d$ transition metals, the neighbouring magnetic ions. The magnetic symmetry of some ($MnSn_2$ [3]) or all ($FeSn_2$ [4]) of the Sn sites is such that the isotropic contribution cancels, leading to a transferred hyperfine field that is totally anisotropic. Table 1.1 lists the measured hyperfine fields in $MnSn_2$ and $FeSn_2$. In $MnSn_2$, the Sn_{00} site is the only site for which the isotropic field cancels. By comparing this anisotropic field to the overall transferred B_{hf} at the other Sn sites (which includes both isotropic and anisotropic contributions), we see that the anisotropic field is a significant fraction of the total B_{hf}. The anisotropic contribution can also be expected to be as important in systems similar to $MnSn_2$ and $FeSn_2$.

The hexagonal $HfFe_6Ge_6$-type crystal structure of $RMn_6Sn_{6-x}X_x$ and $RFe_6Sn_{6-x}X_x$ (R = rare earth; X = Ga, In dopant) is characterized by relatively close $3d$–Sn contacts (through short Mn–Sn bonds), leading to a significant anisotropic contribution. The crystal and magnetic symmetries [5][6] are such that there is no cancelation of the isotropic field at any of the Sn sites. As a result, the Sn sites in $RMn_6Sn_{6-x}X_x$ see contributions that are both isotropic and anisotropic (as was the case for three of the four Sn sites in $MnSn_2$, Table 1.1). A measurement of the hyperfine field cannot distinguish one contribution from the other unless a process is imposed which induces change in only one of them. One such process is spin reorientation, which is a pure rotation of the magnetic structure relative to the crystal structure. The size of the moments and their distances from the probe site do not change, nor does the magnetic symmetry. Since the isotropic Fermi contact field depends only on the *magnitude* of the magnetic moments and the magnetic symmetry, it cannot change under such a simple rotation of the moments. The anisotropic contribution, on the other hand, depends on the relative orientations of the moments and their connecting bonds, and is therefore changed by the reorientation and can be explicitly determined.

1.2 Spin reorientation in RMn_6Sn_6

Venturini et al. [7] carried out the first study of the thermal variation of the magnetic properties of the RMn_6Sn_6 (R = Sc, Y, Gd-Tm, Lu) series of compounds. Among these compounds it was found that for R = Tb-Ho, a second magnetic transition occured below the Néel point which was related to a reorientation of the easy axis magnetization from the basal plane to the c–axis. This was referred to as a temperature-induced spin reorientation, related to the interplay between the magnetocrystalline anisotropy of the Mn and rare earth sublattices (Sections 1.2.1 and 1.2.2). A spin reorientation can also be induced by applying a large enough magnetic field (Section 1.2.3), first observed in $TbMn_6Sn_6$ by Hu et al. [8], and later studied using neutron scattering [9].

1.2.1 Magnetocrystalline anisotropy

The magnetization in ferromagnetic crystals will tend to align along a preferred crystallographic axis, known as the *easy* axis because it is easiest to bring a demagnetized sample to saturation magnetization if the external field is applied along this axis [10]. The tendency of the magnetization to prefer an axis is referred to as the magnetocrystalline anisotropy and it reflects the lowest energy configuration of the magnetic moments. On an atomic scale, the magnetocrystalline anisotropy arises through the spin-orbit coupling of the orbital states that are stabilized by the electrostatic field (crystal electric field) [11]. As the magnetic spins are coupled to the orbitals, and the orbitals themselves strongly coupled to the crystal lattice, then the spins in turn are coupled to crystal axes in the lattice, thereby introducing the anisotropy.

The crystal field Hamiltonian at a rare earth site comes from the Coulomb interaction between the charge distribution in the $4f$ shell and the potential created by the rest of the crystal. The crystal field parameter B_n^m combines the lattice potential and the shape of the charge distribution of the $4f$ shell (oblate or elongated). In general, the second order crystal field parameter (B_2^0) is the leading term in the crystal field Hamiltonian, and the sign of B_2^0 will determine the easy direction: negative B_2^0 favors an easy axis anisotropy, and positive B_2^0 favors an easy plane anisotropy (Table 1.2).

In all compounds, the magnetocrystalline anisotropy decreases with increasing temperature, and near the critical temperature T_c, there is no preferred orientation

Ion	B_2^0 (K)	θ
Tb^{3+}	-0.57	0°
Dy^{3+}	-0.34	45°
Ho^{3+}	-0.11	48°
Er^{3+}	$+0.12$	90°

Table 1.2: Crystal field parameters for several rare earth ions in $\mathrm{RMn_6Sn_6}$. The sign of B_2^0 determines whether the anisotropy is easy axis ($-$) or easy plane ($+$). The angle θ represents the canting angle of the magnetization from the $c-$axis [5].

for domain magnetization. The materials investigated in this study all possess magnetocrystalline anisotropy, and it will simply be referred to as *anisotropy.*

1.2.2 Temperature-induced spin reorientation

At room temperature in antiferromagnetic HfMn$_6$Sn$_6$, the Mn moments lie in the $ab-$plane. The Mn sublattice is said to have *easy plane anisotropy,* meaning that the lowest energy configuration of the magnetic structure is with the moments in the $ab-$plane. In ferrimagnetic TbMn$_6$Sn$_6$ at room temperature, the Tb and Mn moments lie along the $c-$axis. The Tb sublattice therefore has *easy axis anisotropy* (along c) which dominates over the easy plane anisotropy of the Mn sublattice. The Tb sublattice anisotropy has the stronger temperature dependence, and decreases more rapidly on heating. At T$_{sr}$ = 330 K [7], the two sublattice anisotropies are equal, and above T$_{sr}$ the planar Mn anisotropy dominates. The switch in dominant anisotropy causes the Tb and Mn moments to undergo a spontaneous reorientation from the $c-$axis to the $ab-$plane (on heating through T$_{sr}$).

The simple competition between the two sublattice anisotropies is a valid description of the spin reorientation, because the temperature range in which it occurs is rather near to the ordering temperature (T$_N$ = 423 K). At high temperatures, only the second order crystal field parameter B_2^0 contributes significantly, as higher order terms fall off much more rapidly with temperature. The Mn and Tb sublattices have positive and negative B_2^0 parameters, respectively, and the two compete for dominance. If the spin reorientation were to occur at very low temperatures where higher order terms are important, then a switch from B_2^0 dominance to B_4^0 dominance will induce a spin reorientation if the two have opposite signs. For example, the spin reorientation temperatures in the Dy and Ho ternary stannides are T$_{sr}$ = 33 K and 200 K, respectively, whereas the Néel points are T$_N$ = 393 K and 376 K. Neutron diffraction studies have shown that the peculiar behaviour of their magnetic properties is a result of a competition between second and fourth order crystal field parameters [12].

Furthermore, the spin reorientation in these two compounds is incomplete [5][13]. As the spin reorientations in these cases are an effect of the rare earth sublattice only (rather than as a consequence of a competition between rare earth and Mn sublattice anisotropies), the behaviour may not be as simple as the temperature-induced spin reorientation in $\mathrm{TbMn_6Sn_6}$.

1.2.3 Field-induced spin reorientation (spin-flop)

If the spin system is to rotate, the orbitals also must rotate due to the spin-orbit coupling. However, there is a strong coupling between the crystal lattice and the orbitals, and a rotation of the spin axis away from the easy direction is resisted [14]. In order to force the magnetic moments to rotate in response to an applied field, the field must be large enough to overcome this resistance. Once this field is achieved, the moments will rotate towards the direction along which the field is applied. If a new local minimum is found, the moments will spontaneously undergo a spin-flop in order to minimize energy.

1.3 Crystal structure of $\mathrm{TbMn_6Sn_6}$

The $\mathrm{TbMn_6Sn_6}$ system has a $\mathrm{HfFe_6Ge_6}$-type, $P6/mmm$ crystal structure (Figure 1.1), with lattice parameters $a = 5.53(1)$ Å and $c = 9.023(2)$ Å [15]. The Tb atom is in the Tb$-1a$ site at (0,0,0), and the six Mn atoms sit in the Mn$-6i$ sites. There are three Sn sites in the structure: Sn$-2c$, Sn$-2d$ and Sn$-2e$. The coordinates of the atoms in the $\mathrm{TbMn_6Sn_6}$ structure are listed in Table 1.3. Sn$-2c$ and Sn$-2d$ both sit in the center of hexagonal $\mathrm{Mn_6}$ prisms, with Sn$-2c$ surrounded by three Tb neighbours and Sn$-2d$ having none. An alternate site description is with Tb in the Tb$-1b$ site at (0, 0, 1/2), so that Sn$-2d$ is then in the plane of three Tb neighbours instead of Sn$-2c$ [15][16]. The Sn$-2e$ site is distinct, slightly offset from a hexagonal plane of six Mn neighbours, with one Tb above and another Sn$-2e$ below.

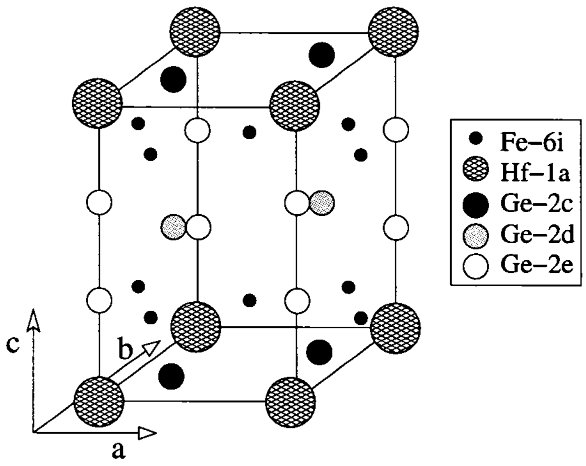

Figure 1.1: $HfFe_6Ge_6$-type crystal structure, which is in the $P6/mmm$ space group. There are three Ge sites in this structure, and Hf and Fe have one site each.

Atom (site)	x	y	z	d (Mn–Sn)
Tb–1a	0	0	0	-
Mn–6i	1/2	0	0.2475(2)	-
Sn–2c	1/3	2/3	0	2.74 Å
Sn–2d	1/3	2/3	1/2	2.78 Å
Sn–2e	0	0	0.3376(1)	2.88 Å

Table 1.3: Coordinates of atoms in the $HfFe_6Ge_6$-type structure of $TbMn_6Sn_6$ [15]. The Mn–Sn bond lengths are given by d.

1.4 Magnetic structure of $TbMn_6Sn_6$

It is simpler first to discuss the antiferromagnetic structure of $HfMn_6Sn_6$, where non-magnetic Hf replaces magnetic Tb. The ordering temperature is $T_N = 575$ K. The Mn sublattice has planar anisotropy, and thus the Mn moments are oriented in the ab–plane. The atoms are layered along c as Hf–Mn–Mn–Hf–Mn–Mn. Strong ferromagnetic interactions ($\mathbf{J}_1$) within the Mn–Mn slab force the moments in the slab to be parallel. The weakly ferromagnetic interaction ($\mathbf{J}_2$) in the Mn–Hf–Mn slab is overwhelmed by the antiferromagnetic interaction ($\mathbf{J}_3$) from the next-nearest Mn neighbours [17]. As a result, ferromagnetic Mn slabs (separated by Hf layers) are

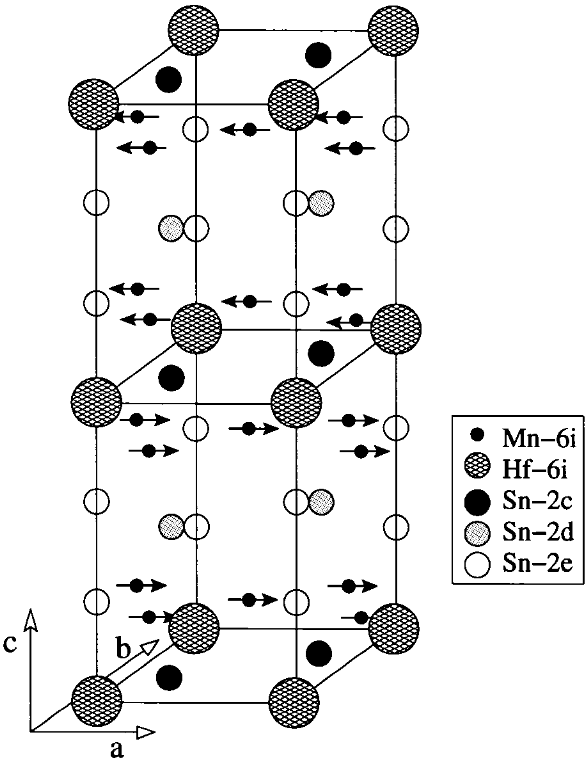

Figure 1.2: Antiferromagnetic structure of $HfMn_6Sn_6$, below T_N = 575 K.

antiferromagnetically coupled, leading to a sequence of moments

$$\text{Hf–Mn}(\leftarrow)\text{Mn}(\leftarrow)\text{–Hf–Mn}(\rightarrow)\text{Mn}(\rightarrow)$$

along the c–axis (Figure 1.2) and an overall antiferromagnetic structure. The Sn–2c site sits in the plane of the Hf layer, so the Mn moments above Sn–2c are antiparallel to those below it (Figure 1.3). As a result, there is no net transferred hyperfine field at Sn–2c. The Sn–2d site is offset from Sn–2c, and lies between two ferromagnetic sheets so that the Mn moments above and below it are parallel. Therefore, the fields add at Sn–2d and result in a large transferred hyperfine field. Finally, Sn–2e is near to a single Mn sheet, so all of the Mn moments are parallel. This also yields a significant hyperfine field at Sn–2e due to the different Mn environment.

When the Hf site is filled with a magnetic moment such as Tb, the magnetic structure is no longer antiferromagnetic. The ordering temperature is T_N = 423 K

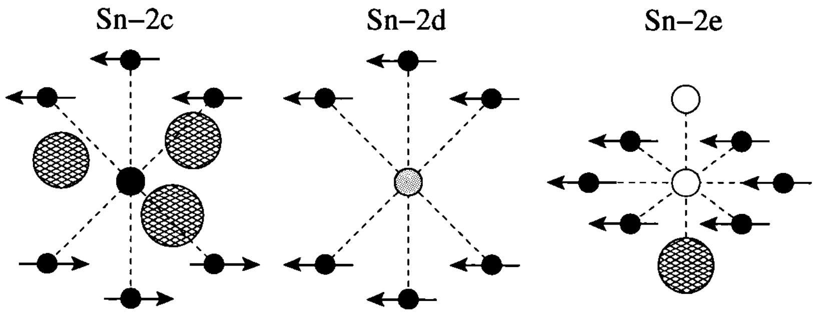

Figure 1.3: Orientation of the Mn moments surrounding the three Sn sites in $HfMn_6Sn_6$, which leads to a cancelation of the hyperfine field at Sn−2*c*, in contrast to Sn−2*d* and Sn−2*e*.

[7]. As the Tb–Mn interactions are stronger than Mn–Mn, the Mn moments prefer to be antiparallel to Tb, and antiferromagnetic coupling is introduced within the Mn–Tb–Mn slab. All of the Mn moments are now parallel within the structure. Since the formerly anti-parallel arrangement of Mn moments in the Mn–Tb–Mn slab is now parallel, the result is a non-zero transferred hyperfine field at Sn−2*c* (Figure 1.4). Just below the ordering temperature, the Mn sublattice anisotropy dominates over Tb, so the Mn and Tb moments are ordered in the *ab*−plane and stacked along *c* as

$$\mathrm{Tb}(\rightarrow)\text{-}\mathrm{Mn}(\leftarrow)\text{-}\mathrm{Mn}(\leftarrow)\text{-}\mathrm{Tb}(\rightarrow)\text{-}\mathrm{Mn}(\leftarrow)\text{-}\mathrm{Mn}(\leftarrow)$$

The structure is ferrimagnetic, which means that the exchange interaction between adjacent magnetic ions (Mn and Tb) leads to an antiparallel alignment of their moments [18] (Figure 1.5, left). This does not lead to antiferromagnetism because the magnetization of one sublattice exceeds that of the other. Cooling through T_{sr} = 330 K causes the moments to spontaneously reorient onto the *c*−axis, because below T_{sr} the uniaxial anisotropy of the Tb sublattice dominates [19] (Figure 1.5, right).

1.5 Summary of RMn_6Sn_6 magnetic properties

The RMn_6Sn_6 family of compounds possesses a rich variety of magnetic properties. Most commonly, the rare earth and Mn sublattices show simultaneous ferromagnetic

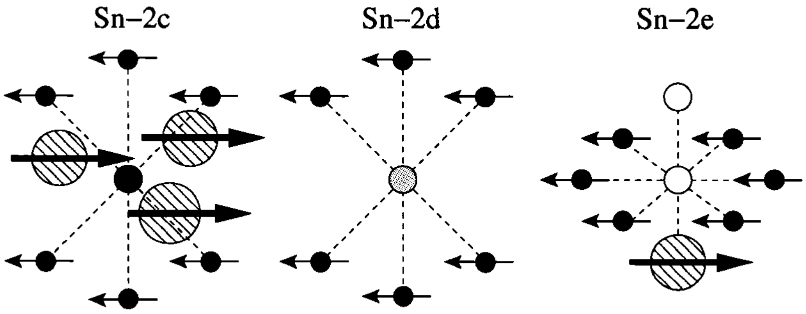

Figure 1.4: Orientation of the Mn and Tb moments surrounding the three Sn sites in $TbMn_6Sn_6$ for $T_{sr} < T < T_N$. There is no cancelation of the hyperfine field at Sn–2*c*, because the antiparallel Tb moments force the moments in the Mn layers to be parallel.

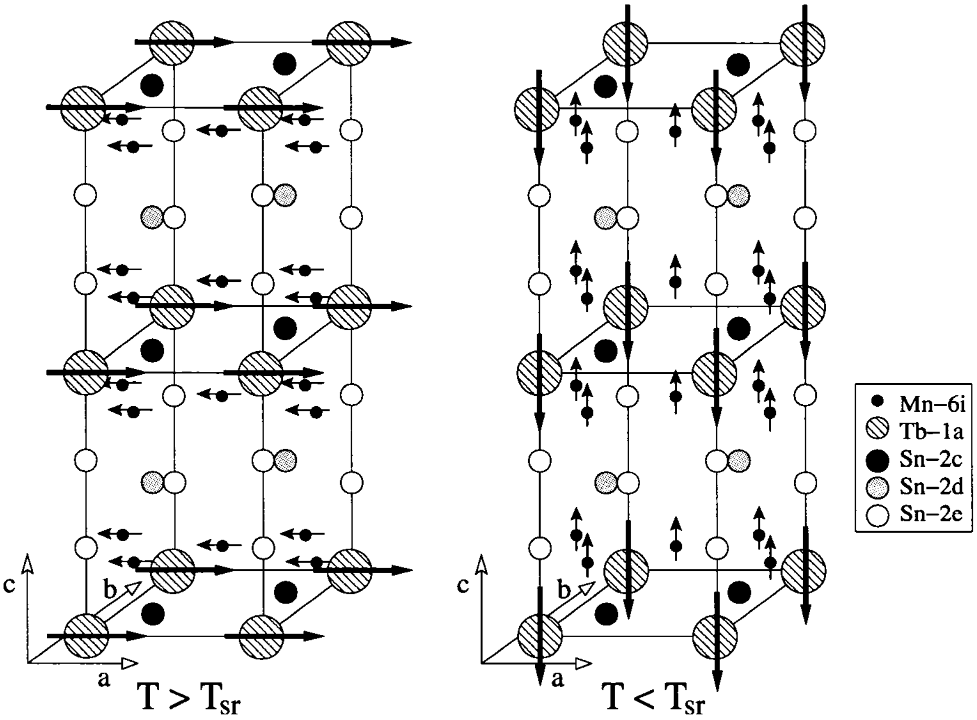

Figure 1.5: Crystal and magnetic structure of $TbMn_6Sn_6$ for temperatures above (left) and below (right) the reorientation temperature, $T_{sr} = 330$ K.

ordering, and the antiferromagnetic coupling between the lattices forces the structure to be ferrimagnetic (R = Gd, Tb, Dy and Ho; Er and Tm are also ferrimagnetic but the rare earth and Mn sublattices do not order simultaneously). In the diamagnetic rare earth compounds, the Mn sublattice orders antiferromagnetically, and in some

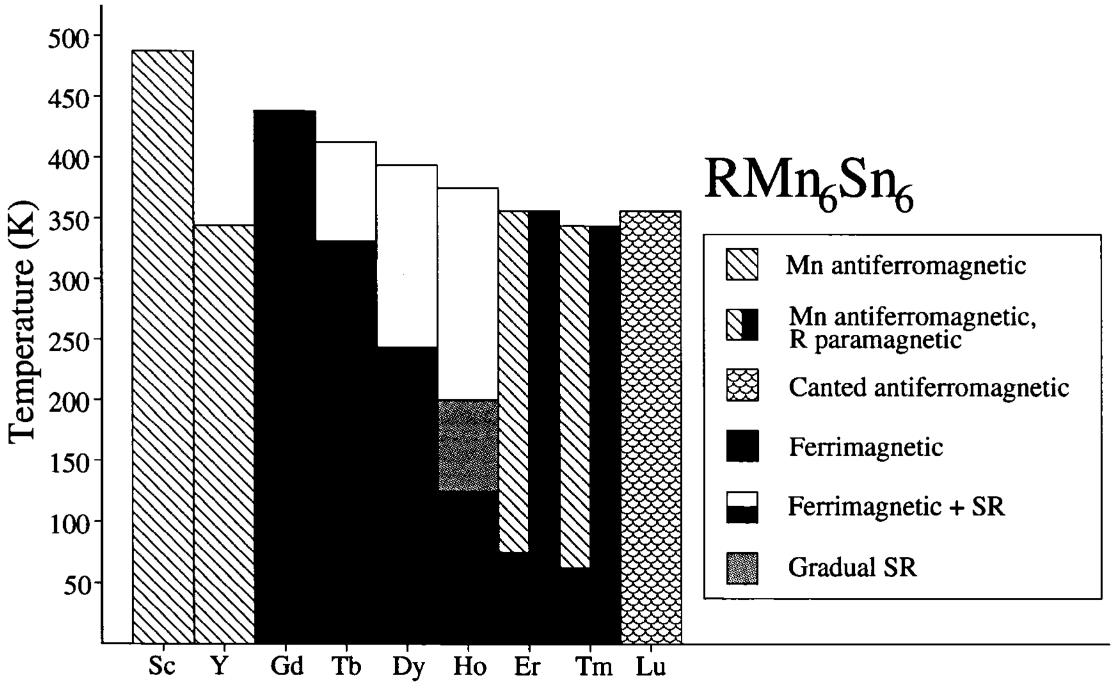

Figure 1.6: Temperature dependence of the various magnetic structures in RMn_6Sn_6. For the Ho compound, the moments gradually rotate between 125 K and 200 K. The Lu compound is canted below $T_N = 353$ K.

cases the structure is canted (YMn_6Sn_6 [7]). Figure 1.6 shows the temperature ranges of the various magnetic structures in most of the studied ternary rare earth stannides, as well as the spin reorientation observed in the Tb-Ho compounds.

In $DyMn_6Sn_6$ and $HoMn_6Sn_6$, the spin reorientation process is not complete [5]. The moments in the Ho compound at 4.2 K deviate from the c–axis by 50°, and gradually rotate into the ab–plane between 125 K and 200 K (see Figure 1.6). In the special cases of helimagnetic Er and Tm, the rare earth sublattices undergo a paramagnetic to ferromagnetic transition at a much lower temperature than the Mn ordering temperature (at 75 K and 58 K for Er and Tm). Below this transition temperature, the structure is ferrimagnetic.

1.6 Role of Ga, In doping

In the $RMn_6Sn_{6-x}X_x$ compounds with paramagnetic rare earths, the main effect of the Ga or In substitution is the modification of the relative strengths of the $\mathbf{J}_2$ and $\mathbf{J}_3$ interactions ($\mathbf{J}_2$ is the weak ferromagnetic interaction in the Mn–R–Mn slab and $\mathbf{J}_3$ is the antiferromagnetic interaction from next nearest Mn neighbours) [17]. The result of the change in $\mathbf{J}_2$ and $\mathbf{J}_3$ is the enhancement of the overall ferromagnetic character of the Mn sublattice. This is supported by observations in the $RMn_6T_{6-x}X_x$ systems (R = Sc, Y, Lu; T = Ge, Sn; X = Ga, In), which all undergo a paramagnetic to ferromagnetic transition above a critical X concentration, x_{crit} [20]. For $LuMn_6Sn_{6-x}In_x$, this critical value is $x_{crit} = 1.2$ [21].

For the paramagnetic rare earths, the x_{crit} values are much lower. The ternary Gd, Tb, Dy and Ho stannides, for example, are ferrimagnetic over their whole ordered range, thus $x_{crit} = 0$. In the helimagnetic Er and Tm compounds, the enhancement of global ferromagnetic character results from increasing In doping levels, thereby increasing the temperature at which the compounds become ferrimagnetic. Above the critical In concentration ($x_{crit} = 0.5$ for Tm and $x_{crit} = 0.2$ for Er), the compounds are ferrimagnetic in their whole ordered range [22]. The decrease in x_{crit} on going from Tm to Gd is related to increased R–Mn interactions for decreasing rare earth atomic radius [17].

For In concentrations just below x_{crit} in the Er and Tm compounds, there are several magnetic transitions: two ferrimagnetic and one antiferromagnetic. The ordering temperatures are shown in Table 1.4 for $TmMn_6Sn_{5.6}In_{0.4}$ and $ErMn_6Sn_{5.9}In_{0.1}$. The final ferrimagnetic transition is referred to as re-entrant ferrimagnetism [22].

The observations made in the $RMn_6Sn_{6-x}X_x$ systems (X = Ga, In) show that Ga substitution plays a predominant role on the magnetocrystalline anisotropy. A general decrease in spin reorientation temperature (in the Tb, Dy and Ho compounds) resulting from increased Ga doping levels indicates that either the anisotropy of the Mn sublattice is enhanced by larger x, or that the Tb sublattice anisotropy suffers.

	Ordering temperature (K)	
Magnetic structure	$TmMn_6Sn_{5.6}In_{0.4}$	$ErMn_6Sn_{5.9}In_{0.1}$
Ferrimagnetic	322	342
Antiferromagnetic	264	319
Ferrimagnetic	111	141
x_{crit}	0.5	0.2

Table 1.4: Ordering temperatures in the $TmMn_6Sn_{5.6}In_{0.4}$ and $ErMn_6Sn_{5.9}In_{0.1}$ compounds, for In concentrations just below x_{crit}. The final transition is referred to as re-entrant ferrimagnetism. Results from [22].

At high Ga concentrations in $TbMn_6Sn_{6-x}Ga_x$ ($x \geq 1$), the Tb and Mn moments are in the ab−plane for the whole ordered range, indicating that the Mn anisotropy dominates at all temperatures, again either because it is enhanced by the substitution or because the Tb anisotropy is severely reduced. In this case, no spin reorientation is observed. In [12], an example is shown for $TbMn_6Sn_6Ga$.

Table 1.5 summarizes the easy directions of the magnetization (magnetocrystalline anisotropy) in most of the $RMn_6T_{6-x}X_x$ compounds (T = Ge, Sn; X = Ga, In) investigated thus far, and how they relate to Ga and In doping rates. A critical dopant concentration changes the magnetocrystalline anisotropy by changing the sign of the crystal field parameter of one of the sublattices. The sign change of B_2^0 results in a change from easy axis to easy plane (or vice versa) and thus a spin reorientation.

	Tb	Dy	Ho	Er	Tm	Lu
RMn_6Sn_6	Easy-axis	Cone	Cone	Easy-plane	-	-
$RMn_6Sn_{5.5}In_{0.5}$	Easy-axis	Cone	Cone	Easy-plane	Easy-plane	Easy-plane ($x = 1.4$)
$RMn_6Ge_{5.3}Ga_{0.7}$	Easy-axis	Cone	Cone	Easy-axis	Easy-axis	-
$RMn_6Ge_{5.2}Ga_{0.8}$	Easy-axis	Cone	Cone	Easy-axis	Easy-axis	Easy-plane ($x = 1.0$)
$RMn_6Sn_{4.9}Ga_{1.1}$	Easy-plane	Cone	Cone	Easy-axis	Easy-axis	Easy-plane ($x = 1.9$)

Table 1.5: Easy magnetization directions measured at 4.2 K in $RMn_6T_{6-x}X_x$ compounds (T = Sn, Ge; X = Ga, In) [17].

Figure 1.7 shows the relation between spin reorientation temperature and dopant concentration in $TbMn_6Sn_{6-x}X_x$ (X = Ga, In) (Chapter 3 and [19]). While increased Ga concentrations strongly reduce T_{sr}, the effect of In substitution is much weaker (T_{sr} is nearly constant throughout the composition range of $0.2 \leq x \leq 0.8$), indicating that the substitution of In for Sn does not change the magnetocrystalline anisotropy of the sublattices in $TbMn_6Sn_{6-x}In_x$. This observation is consistent through the series of rare earth compounds (R = Tb, Dy and Ho).

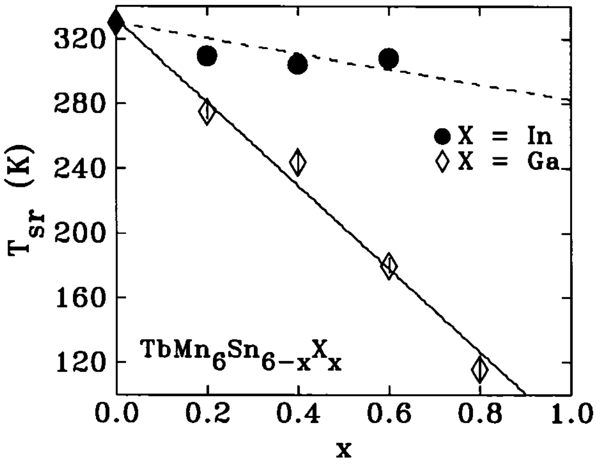

Figure 1.7: Effect of Ga or In substitution on the spin reorientation temperature in $TbMn_6Sn_{6-x}X_x$ (X = Ga, In). The results for $TbMn_6Sn_{6-x}Ga_x$ are discussed in Chapter 3 while those for $TbMn_6Sn_{6-x}In_x$ are from [19].

1.7 Site preference for X substitution

The neutron diffraction study of $TmMn_6Sn_{6-x}Ga_x$ (x = 2.0 and 2.5) [23] showed a significant increase in occupancy factor corresponding to the Sn−2*c* site. Owing to the relative neutron scattering lengths of Sn and Ga, this means that the Ga atoms are substituting on the Sn−2*c* site. This was reinforced by an x-ray single crystal study of $TmMn_6Sn_{6-x}Ga_x$ (x = 1.2 and 2.6) [24], which showed a reduction in occupancy factor at Sn−2*c* and, to a lesser degree, at Sn−2*d*, confirming that the Ga atoms substitute at Sn−2*c*. The substitution also occurs at Sn−2*d*, but in smaller quantities.

We can also investigate the Ga site preference by considering Sn site volumes for samples with lower Ga doping levels than those studied through neutron and x-ray diffraction ($x < 1.2$). In Figure 1.8 (left), the volumes of the three Sn sites in $RMn_6Sn_{6-x}Ga_x$ (R = Tm, Tb) are shown for $0 \leq x \leq 2.5$. Sn$-2c$ is the smallest of the three Sn sites. The site volumes were obtained using BLOKJE [25] and cell parameters from [12][23]. On the right-hand side of Figure 1.8, we show the percent change in site volume in response to doping, $\Delta V(\%)$:

$$\Delta V(\%) = \frac{V_x - V_0}{V_x} \times 100 \tag{1.2}$$

where V_x is the site volume for a given x composition and V_0 is that of the ternary compound. In Figure 1.8 (right), all ΔV values are negative, as the site volumes decrease when Sn (17.81 Å^3) is replaced with the smaller Ga (11.74 Å^3).

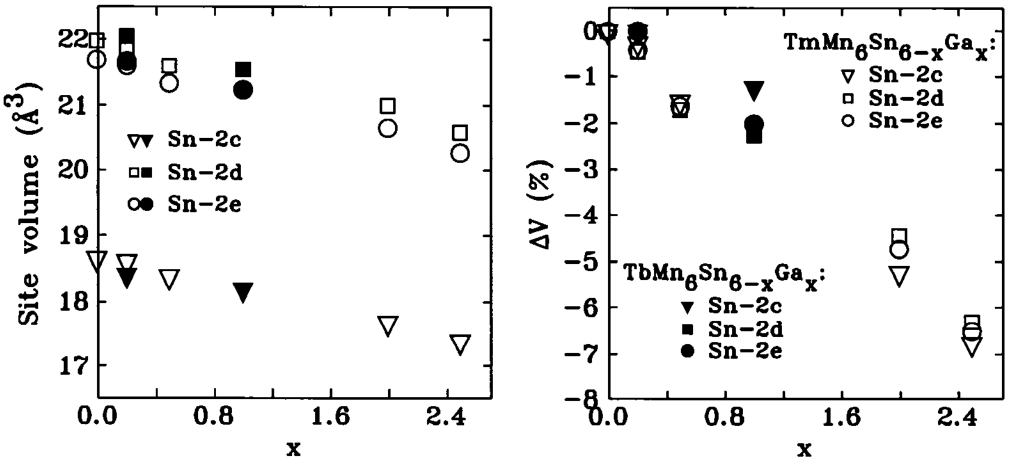

Figure 1.8: Left: Sn site volumes in $TmMn_6Sn_{6-x}Ga_x$ (open symbols) and $TbMn_6Sn_{6-x}Ga_x$ (closed symbols). Right: Percent change in site volume (ΔV) for the Tm and Tb compounds described above, which is negative because Sn is replaced with smaller Ga atoms, thereby decreasing the site volume. Cell volumes were calculated using parameters from [12][23] and BLOKJE [25].

In $TmMn_6Sn_{5.8}Ga_{0.2}$ and $TmMn_6Sn_{5.5}Ga_{0.5}$, the three Sn sites have nearly equal ΔV values, meaning that the volume of each Sn site decreases by the same amount in response to Ga substitution, and thus there is no clear site preference for $x \leq 0.5$. In $TmMn_6Sn_4Ga_2$ and $TmMn_6Sn_{3.5}Ga_{2.5}$, ΔV for Sn$-2c$ is the most negative. Since

Ga is smaller than Sn, this suggests that Ga atoms substitute mostly at Sn$-2c$ in $\mathrm{TmMn_6Sn_{6-x}Ga_x}$ for $x \geq 2$, in agreement with the site preference determined through neutron scattering.

By contrast, in $\mathrm{TbMn_6Sn_{5.2}Ga_{0.8}}$, the Sn$-2d$ site volume decreases the most in response to Ga substitution (largest $-\Delta V$), while the Sn$-2c$ site volume decreases the least (smallest $-\Delta V$). This suggests that Ga atoms substitute mostly at the Sn$-2d$ site, and show a slight preference for Sn$-2e$, in Tb compounds with low Ga doping ($x < 1$). This contradicts the site preference determined through neutron scattering, but is fully consistent with our recent Mössbauer study of $\mathrm{TbMn_6Sn_{6-x}Ga_x}$ ($0.2 \leq x \leq 0.8$) compounds [16]. Since different doping levels give different site preferences, further Mössbauer studies on a series of substituted compounds such as $\mathrm{YMn_6Sn_{6-x}Ga_x}$ and $\mathrm{TbMn_6Sn_{6-x}In_x}$, as well as neutron scattering studies of $\mathrm{RMn_6Sn_{6-x}Ga_x}$ compounds with lower x (< 2), should provide insight into the Ga site preference.

Purpose of the study

We present here the results for the temperature-induced spin reorientations in the $\mathrm{ErMn_6Sn_{5.89}Ga_{0.11}}$ and $\mathrm{TbMn_6Sn_{6-x}Ga_x}$ powders, and the field-induced spin-flop in $\mathrm{TbMn_6Sn_{5.46}In_{0.54}}$ single crystals. We show that the spin reorientation is a 90° rotation of the magnetic moments, and that the driving force of the reorientation does not change the anisotropic contribution to the transferred hyperfine field at the Sn sites. This contribution can thus be determined through either method. We show that the anisotropic contribution is large in all cases, and shows some relation to the concentration of the dopant atoms as well as to the choice of rare earth.

Chapter 2

Experimental methods

2.1 Sample preparation

The four $TbMn_6Sn_{6-x}Ga_x$ compounds (x = 0.2, 0.4, 0.6 and 0.8) were prepared by Venturini et al. by alloying stoichiometric amounts of ternary $TbMn_6Sn_6$ and $TbMn_6Ga_6$ in an induction furnace [23]. The resulting ingots were sealed under argon in quartz tubes and annealed for two weeks at 973 K.

The $ErMn_6Sn_{5.89}Ga_{0.11}$ and $TbMn_6Sn_{5.46}In_{0.54}$ single crystals were synthesized using a flux method similar to that previously reported by Clatterbuck et al. [13]. For $ErMn_6Sn_{5.89}Ga_{0.11}$, a mixture of $ErMn_6Sn_6$ and elemental gallium was compacted into pellets and put into a silica tube with a large amount of elemental tin, giving rise to the atomic ratio $ErMn_6Sn_{31.5}Ga_{0.5}$. A quartz-wool stopper was placed in the tube, which was then sealed under argon (200 mm Hg). The same was done for $TbMn_6Sn_{5.46}In_{0.54}$, with a mixture of $TbMn_6Sn_6$, pure tin and indium metal (atomic ratio $TbMn_6Sn_{23}In_{37}$). The silica tube was placed in a furnace and heated to 1273 K (at 50 K/h) for 24 h, after which it was cooled to 1223 K (6 K/h). The sample was then re-heated to 1263 K at the same rate and finally cooled slowly to 873 K in 65 h. The tube was quickly removed from the furnace, inverted and centrifuged manually using a David's sling device. The (Sn,In) flux settled to the bottom of the tube and the

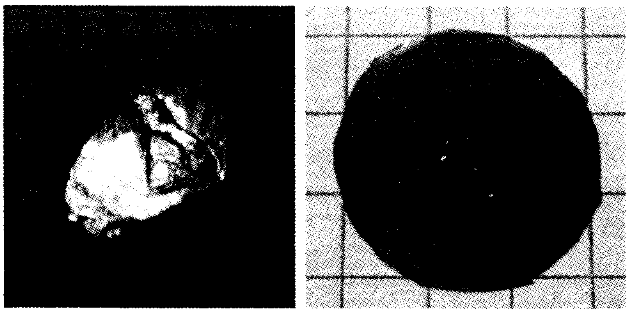

Figure 2.1: Left: $ErMn_6Sn_{5.89}Ga_{0.11}$ single crystal. Right: Arrangement of $TbMn_6Sn_{5.46}In_{0.54}$ single crystal platelets. The magnetic moments are along c, out of the plane of the crystals.

hexagonal crystals remained on the quartz-wool stopper. In the $RMn_6Sn_{6-x}X_x$ series, it was found that the larger the rare earth element, the thinner the crystals. Furthermore, a larger concentration of dopant results in thinner crystals. $ErMn_6Sn_{5.89}Ga_{0.11}$ thus grew as a large single crystal (Figure 2.1, left), and it was powdered for x-ray diffraction and Mössbauer spectroscopy. $TbMn_6Sn_{5.46}In_{0.54}$ single crystals grew as thin platelets (~1-2 mm in diameter and ~60 μm thick), with the c−axis perpendicular to the plane of the plates. The single crystal platelets were sandwiched between two Kapton sheets, and assembled in a mosaïc to make the $TbMn_6Sn_{5.46}In_{0.54}$ sample (Figure 2.1, right). Both compounds are isotypic with the $HfFe_6Ge_6$ structure. The composition of the crystals was verified using a SX50 electron probe at the Service Commun de Sondes Électroniques de l'Université de Nancy I-Henri Poincaré [26].

2.2 Principles of Mössbauer spectroscopy

2.2.1 The Mössbauer effect

When a free atom at rest emits a photon, the nucleus recoils to conserve the total momentum of the system. The recoil momentum p of the nucleus is thus equal and opposite to the momentum of the outgoing γ-ray:

$$p = Mv = -p_\gamma = -\frac{E_\gamma}{c} \tag{2.1}$$

where M is the nuclear mass, v the velocity change the nucleus experiences as a result of the recoil, E_γ the γ-ray energy, and c the velocity of light. The energy lost by the nucleus is the difference between the excited and ground state energies, $E = E_e - E_g$. In order to conserve energy, this energy difference must equal:

$$E = \frac{1}{2}Mv^2 + E_\gamma = \frac{p^2}{2M} + E_\gamma \tag{2.2}$$

Energy conservation thus demands a recoil energy, E_R, given by:

$$E_R = E - E_\gamma = \frac{p^2}{2M} = \frac{E_\gamma^2}{2Mc^2} \tag{2.3}$$

Equation 2.3 shows that there exists an explicit relation between the recoil energy and the energy of the emitted γ-ray.

When the emitting atom is bound in a solid lattice, the recoil mass M is the mass of the lattice as a whole, and E_R in equation 2.3 is significantly reduced. Chemical binding energies in solids are on the order of 10 eV, which is considerably greater than the recoil energy E_R of a free atom (Table 2.1). Otherwise, the atom would be dislodged from the crystal lattice. While the nucleus in a solid cannot recoil freely, it remains free to vibrate. If E_R is similar to the characteristic phonon energy, the recoil energy will be dissipated by means of phonon creation. If however E_R is less than the lowest phonon available to the system, the emission is referred to as *recoilless*, and the energy of the outgoing γ is simply $E_\gamma = E_e - E_g$. When this occurs in both source and absorber, the condition for resonance absorption of γ-rays is satisfied [27]. The recoilless resonant absorption of γ-rays was discovered by Rudolph Mössbauer in 1957, who received the Nobel prize in 1961 for the effect which now bears his name.

2.2.2 ^{119}Sn Mössbauer spectroscopy

In general, a Mössbauer spectrum will consist of many resonance lines, because the electric and magnetic interactions between electrons and nuclei in both the source and absorber shift and split the nuclear levels (Figure 2.2 shows an example of magnetic

Source of energy	Symbol	Range (eV)
Mössbauer γ-ray	E_γ	$10^4 - 10^5$
Chemical binding	E_B	$1 - 10$
Free-atom recoil	E_R	$10^{-1} - 10^{-4}$
Lattice vibrations (phonons)		$10^{-1} - 10^{-3}$
Heisenberg natural linewidth	Γ_s	$10^{-6} - 10^{-9}$

Table 2.1: Typical energies associated with the Mössbauer effect [28].

splitting for the $\frac{3}{2} \rightarrow \frac{1}{2}$ transition in ^{119}Sn). The study of these interactions, known as hyperfine interactions, is the main purpose of Mössbauer spectroscopy, and they are discussed in greater detail in the following sections. The energy shift associated with these interactions is typically on the order of 10^{-6} eV. The absorption lines are

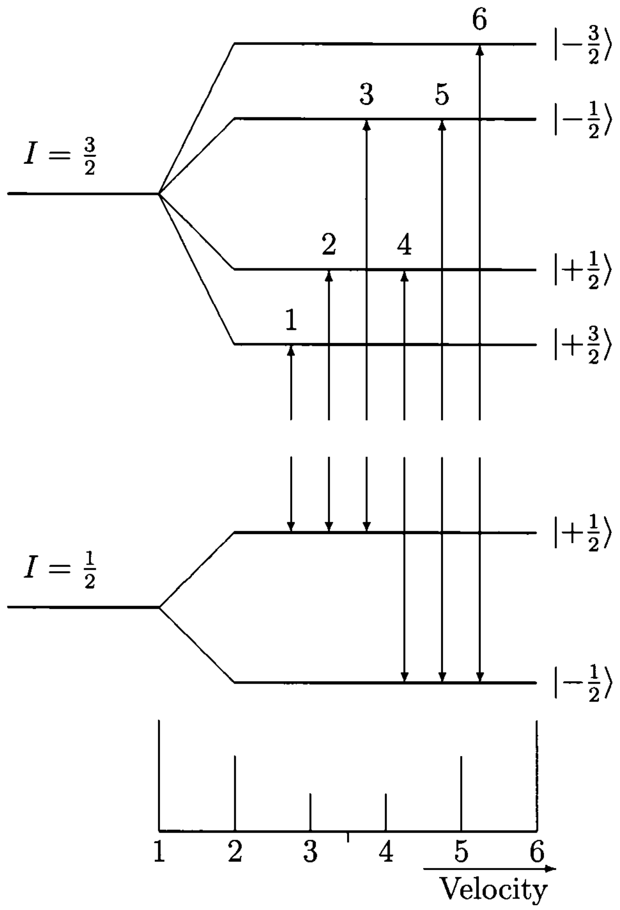

Figure 2.2: Magnetic splitting for the $\frac{3}{2} \rightarrow \frac{1}{2}$ transition in ^{119}Sn. The only allowed transitions are for a change in m of 0 or ± 1, giving a six line Mössbauer pattern [29].

Lorentzian, and the line width (Γ) is inversely proportional to the mean lifetime of the excited state (τ) [30]. The Heisenberg natural linewidth is given by $\Delta E \Delta \Gamma_s = \frac{\hbar}{2}$, and natural linewidths (given in Table 2.1) are typically smaller than the energy shift caused by hyperfine interactions. The possibility of resonant absorption is therefore lost, caused by the very interactions which are most meaningful in a Mössbauer study. If the γ-ray source is Doppler shifted, then the energy range of the outgoing γ-rays encompasses that of the shift between energy states, and resonant absorption can occur when the incident and absorber energies match. The Doppler shift energy is given by:

$$\Delta E = \frac{v}{c} E_\gamma \tag{2.4}$$

where v is Doppler velocity of the source. With this approach, the resulting Mössbauer spectrum has velocity in mm/s on the x-axis, instead of energy. The natural linewidth of Sn foil (from ^{119}Sn Mössbauer spectroscopy) is approximately 0.470(2) mm/s.

There are several approaches to Mössbauer spectroscopy. The most popular is the transmission mode, with the sample between the source and detector. This is the approach used throughout this work, and an example of the setup is shown in Figure 2.3. The setup consists of a γ-ray source, a detector, and a mechanical drive, and all are part of the spectrometer. The source is attached to an electromechanical transducer or drive, which is usually driven trapezoidally to give the desired Doppler shift and Mössbauer absorption spectrum. Typical drive velocities for ^{119}Sn are ± 30 mm/s. Since in the transmission mode the detector counts the γ-rays that were not absorbed by the sample, it is the loss in incident counts which is plotted against velocity to give the absorption spectrum. Therefore the spectral lines point downwards. Other Mössbauer spectroscopy approaches are γ-ray backscattering, x-ray backscattering, and conversion electron Mössbauer spectroscopy, which all are backscattering methods. This approach yields emission spectra consisting of γ-radiation that has been re-emitted from the sample. In these cases, the lines in the spectra are emission lines, which point upwards.

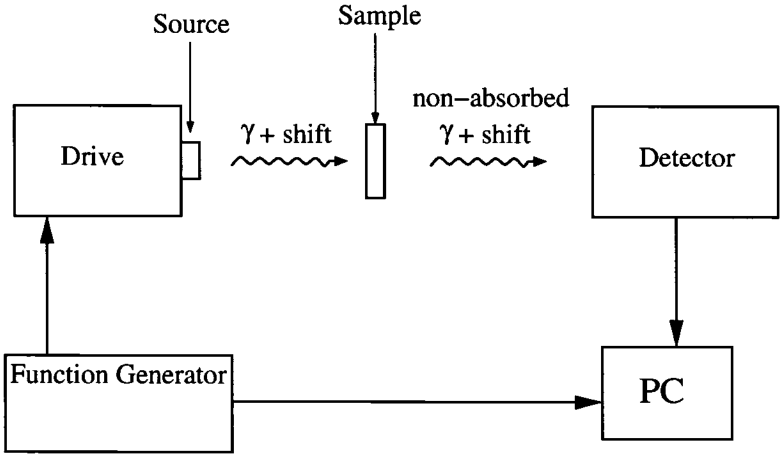

Figure 2.3: Mössbauer drive, source, sample and detector. The Mössbauer source is mounted on the drive [31].

Mössbauer source, spectrometer and detectors

The Mössbauer source used in this study was a 10 mCi ^{119m}Sn CaSnO3 source, whose decay scheme is shown in Figure 2.4. A 25 μm Pd filter is added to the spectrometer's snout (just beyond the source) because the energy of the Sn-K_α x-ray, also emitted by the source, is very near to the Sn-γ used in the experiment, and it must be filtered to avoid interference. ^{119}Sn Mössbauer spectra were obtained using this source and two detectors: a NaI scintillation (photomultiplier) detector (Figure 2.5, right), and a 2

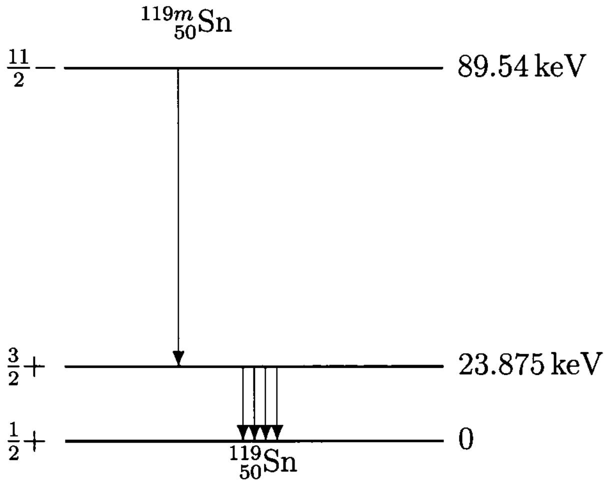

Figure 2.4: ^{119}Sn decay scheme. The energy of the ^{119}Sn Mössbauer γ is 23.875 keV.

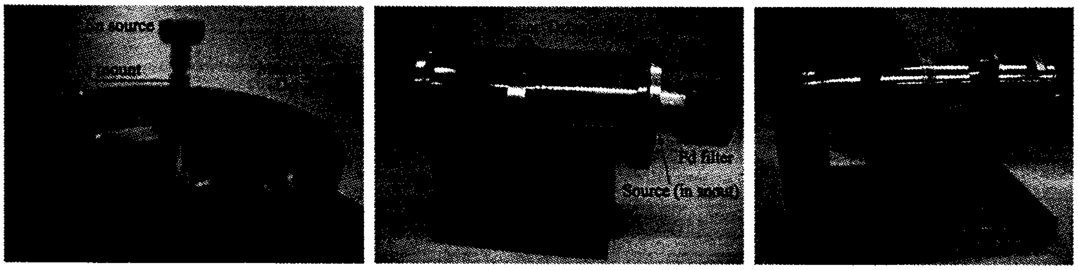

Figure 2.5: Left: ^{119}Sn Mössbauer source, mounted on a loud-speaker in the Mössbauer spectrometer. Middle: Mössbauer spectrometer. The source is mounted within the snout, and a 25 μm Pd filter is placed on the snout to eliminate the contaminant Sn-K_α signal. Right: NaI scintillation detector.

atm Xe/CO$_2$ proportional counter. Both detectors show a linear relationship between photon output and initial (input) γ-ray energy for E$_\gamma$ > 10 keV (the ^{119}Sn γ has E_γ = 23.875 keV). The NaI detector is the more efficient detector, but it is switched to the proportional counter for the in-field measurements of TbMn$_6$Sn$_{5.46}$In$_{0.54}$ because the external field would affect the photomultiplier tube within. It is however the standard detector used in γ-ray spectroscopy [32]. The source, spectrometer and detector are shown in Figure 2.5.

2.2.3 Debye-Waller factor and Debye temperature θ_D

Since recoilless γ-ray resonant absorption is key in the Mössbauer effect, we define f as the proportion of events that are resonantly absorbed with respect to the total number of γ events. This fraction is known as the recoil-free fraction, or alternatively the probability of zero-phonon events, as both effects guarantee that $E_\gamma = E_e - E_g$. The recoil-free fraction depends on the free atom recoil energy ($\propto E_\gamma^2$), on the properties of the solid lattice, and on the temperature of the sample. As the forces acting within the nucleus are extremely short ranged compared to those which hold the lattice together, the nuclear decay is independent of vibrational state, and conversely, the vibrational state is independent of the nuclear decay. The probability of recoilless emissions is reduced to:

$$f = const \times \mid \langle L_f \mid e^{i\mathbf{k}.\mathbf{x}} \mid L_i \rangle \mid^2 \tag{2.5}$$

where L_i is the initial vibrational state (note that for recoilless emission $L_i = L_f$), $\mathbf{k} = p/\hbar$ is the wavevector for the emitted γ-ray and $\mathbf{x}$ is the coordinate vector of the center of mass of the decaying nucleus [33]. Since L_i is normalized, equation 2.5 becomes:

$$f = e^{-\mathbf{k}\cdot\mathbf{x}} \tag{2.6}$$

The Debye model abandons the concept of a single vibrational frequency. The model instead assumes a continuum of oscillator frequencies with maximum ω_D, and follows the distribution formula $N(\omega) = \text{const} \times \omega^2$. We may define a characteristic *Debye temperature* θ_D as $\hbar\omega_D = k\theta_D$ [34]. The Debye model then leads to:

$$f = exp\left[-\frac{6E_R}{k\theta_D}\left\{\frac{1}{4} + \left(\frac{T}{\theta_D}\right)^2 \int_0^{\theta_D/T} \frac{x\mathrm{d}x}{e^x - 1}\right\}\right] \tag{2.7}$$

In the low temperature approximation corresponding to $T \ll \theta_D$, the recoil-free fraction is given by:

$$f(T) = exp\left[-\frac{3}{2}\frac{E_R}{k\theta_D} - \frac{E_R\pi^2}{k\theta_D^3}T^2\right] \tag{2.8}$$

At $T = 0\ K$,

$$f_0 = exp\left[-\frac{3E_R}{2k\theta_D}\right] \tag{2.9}$$

and finally in the high temperature limit where $T \geq \frac{1}{2}\theta_D$,

$$f(T) = exp\left[-\frac{6E_RT}{k\theta_D^2}\right] \tag{2.10}$$

The area of the resonant absorption lines in a Mössbauer spectrum is determined by the probability of recoilless absorption, and thus relates to the recoil-free fraction. Furthermore, a ^{119}Sn Mössbauer pattern of a Sn-bearing sample with several Sn environments will have a subspectral component for each different Sn environment or site. The subspectral areas represent the distribution of each site in the sample structure. The subspectral area of a site which has a very low f-factor will be under-represented at high temperature, where the probability of recoilless absorption is small. In such a case, the sample must be analyzed at low temperature to get an accurate representation of the environments within it. As seen in equation 2.9, even at 0 K the recoil-free fraction depends on the Debye temperature. The recoil-free fraction can only reliably be determined through a temperature scan from which the Debye temperature can be obtained. In order to calculate the Debye temperature of a Mössbauer spectrum, the natural logarithm of the fraction of absorbed counts is plotted against the temperature (in the high-T limit) or the square of the temperature (in the low-T limit). The slope of the linear fit gives θ_D for either regime. To determine the Debye temperature of a subspectrum, the total absorption is normalized to the subspectral area.

It is useful to calculate the Debye temperature if there is a need to determine the nature of unknown subspectral components in a Mössbauer pattern. An example of this will be seen in Chapter 3, where an elemental Sn impurity appears in the Mössbauer spectra of $\mathrm{ErMn_6Sn_{5.89}Ga_{0.11}}$. In addition, since the Sn atoms in some of the Sn sites in $\mathrm{RMn_6Sn_{6-x}X_x}$ are substituted with Ga or In, there should be a reduction in the Mössbauer subspectral area associated with the site on which the substitution occurs. In order to ensure that this is an effect of site occupancy rather than a decrease in recoil-free fraction, the Debye temperatures for each of the subspectra can be calculated and compared.

2.2.4 Hyperfine interactions

The total interaction Hamiltonian for an atom is given by:

$$\mathcal{H} = \mathcal{H}_\circ + \mathcal{H}_C + \mathcal{H}_M + \mathcal{H}_Q + \ldots \tag{2.11}$$

where $\mathcal{H}_\circ$ refers to all terms in the Hamiltonian except the hyperfine interactions, $\mathcal{H}_C$ the Coulomb interactions (electric monopole), $\mathcal{H}_M$ the magnetic dipole hyperfine

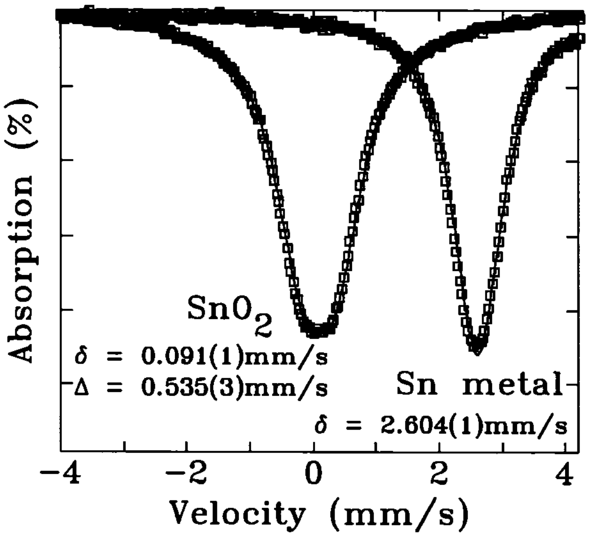

Figure 2.6: Effect of isomer shifts on single Mössbauer resonance lines in Sn metal and SnO$_2$, which reflects the difference in electrostatic environment between the metal and oxide systems.

interactions, and $\mathcal{H}_Q$ the electric quadrupole interactions.

The Coulomb term $\mathcal{H}_C$ changes the separation between the nuclear ground and excited states, and is known as the *isomer shift* [35], because it shifts the resonance lines in a Mössbauer spectrum (Figure 2.6). The isomer shift of elemental Sn from ^{119}Sn Mössbauer spectroscopy is $\delta = 2.56$ mm/s [36].

Quadrupole splitting Δ

Any nucleus with a spin quantum number greater than $I = \frac{1}{2}$ has a non-spherical charge distribution. The magnitude of the charge deformation is known as the nuclear quadrupole moment, Q. The electronic charge distribution is seldom spherically symmetric, resulting in an electric field gradient at the nucleus. This electric field gradient is described by the tensor:

$$E_{ij} = -V_{ij} = -\left(\frac{\delta^2 V}{\delta x_i x_j}\right)(x_i, x_j = x, y, z) \tag{2.12}$$

where V is the electrostatic potential. A coordinate system can be chosen such that the tensor is diagonal, and conventionally, V$_{zz} = eq$ is defined as the maximum so that the orientation of the nuclear axis with respect to the principal axis, z, is quantized [37]. Since the tensor is traceless ($V_{xx} + V_{yy} + V_{zz} = 0$), the quadrupole interaction splits the nuclear energy levels without shifting the center of the resonance lines [38] (Figure 2.7). If we define $\eta = \frac{V_{xx}-V_{yy}}{V_{zz}}$, the tensor can then be entirely specified by two parameters: V_{zz} and η, defined as the asymmetry parameter. The quadrupole splitting is due to interactions of the nuclear quadrupole moment with the electric field gradient, and the Hamiltonian is given by:

$$\mathcal{H}_Q = \frac{eQV_{zz}}{4I(2I-1)}\left[3\hat{I}_z^2 - I(I+1) + \frac{\eta}{2}(\hat{I}_+^2 - \hat{I}_-^2)\right] \tag{2.13}$$

where e is the proton charge, I is the spin, and $\hat{I}_+$ and $\hat{I}_-$ are ladder operators.

As the x-axis of the Mössbauer pattern is velocity in mm/s , obtained by Doppler shifting the energy of the source γ-ray, it is more useful to have a quadrupole component expressed in velocity units. The conversion factor is the velocity shift corresponding to a 1 eV shift in the Hamiltonian of equation 2.13. The quadrupole splitting is expressed as:

$$\Delta = \frac{c}{E_\gamma}\frac{3eQV_{zz}}{4I(2I-1)} \tag{2.14}$$

Typical ^{119}Sn quadrupole splittings vary between 0 mm/s and 3 mm/s. The effect of quadrupole splitting on a single ^{119}Sn Mössbauer resonance line is shown in Figure 2.7.

Hyperfine Field B$_{hf}$

The hyperfine splitting is caused by the interaction of the nuclear magnetic moment with the internal magnetic field generated by the motion of electrons. The hyperfine field is thus to a first approximation assumed to be proportional to the magnetic moment through the relation [39]:

$$\mathrm{B}_{hf} = A_{hf} \cdot \mu \tag{2.15}$$

where A_{hf} is the hyperfine interaction constant and μ the magnetic moment. In α-Fe, $\mathrm{B}_{hf} = -33$ T and $\mu = 2.2\ \mu_B$, giving a hyperfine interaction constant of

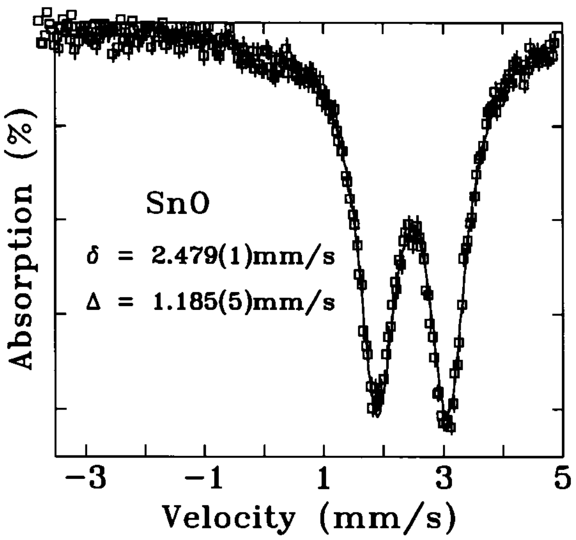

Figure 2.7: Effect of a quadrupole splitting on a ^{119}Sn Mössbauer singlet (along with an isomer shift).

$A_{hf} = -15$ T/μ_B in ^{57}Fe. The sign of B_{hf} cannot be distinguished through Mössbauer spectroscopy, and the hyperfine field in ^{57}Fe is simply 33 T. This hyperfine field splits the nuclear levels, resulting in a six line Mössbauer pattern according to the selection rules on spin.

Continuing with the example of ^{57}Fe, when an external field B_{ext} is applied in the ↑ direction, the Fe moments will align preferentially ↑ along the direction of B_{ext}. The ↑ *d* electrons will induce an ↑ spin imbalance in the *s* electrons of Fe. This induces a ↓ spin imbalance at the Fe nucleus, and thus the ^{57}Fe hyperfine field B_{hf} (↓) is antiparallel to the applied field B_{ext} (↑). The observed hyperfine field is expressed as:

$$|B_{hf}^{obs}| = B_{hf} - B_{ext} \tag{2.16}$$

When the observed hyperfine field is plotted as a function of applied field, the relationship is linear, with a slope of −1 (an example of this is shown in Chapter 5, for the spin-flop of $TbMn_6Sn_{5.46}In_{0.54}$).

In contrast to equation 2.15, it is slightly more accurate to express the hyperfine field as a combination of several fields:

$$\mathrm{B}_{hf} = \mathrm{B}_{cp} + \mathrm{B}_{cond} + \mathrm{B}_{orb} + \mathrm{B}_{dip} \tag{2.17}$$

B_{cp} and B_{cond} represent the spin polarization of core and conduction electrons. B_{orb} and B_{dip} are the anisotropic terms, proportional to the orbital moment or to the dipolar field, respectively [40]. This expression of the hyperfine field is identical to that of the hyperfine field transferred to non-magnetic Sn atoms, shown in equation 1.1 of Chapter 1:

$$\mathbf{B}_{hf} = \left(\mathrm{A}_p \sum_{i=1}^{n} \mathbf{u}_i(\vec{\mu}_i \cdot \mathbf{u}_i) - \frac{\mathrm{A}_p}{3} \sum_{i=1}^{n} \vec{\mu}_i \right) + \mathrm{A}_s \sum_{i=1}^{n} \vec{\mu}_i \tag{2.18}$$

The Sn transferred hyperfine fields in $\mathrm{RMn_6Sn_6}$ compounds vary between 0 T and 34 T, as they depend on the magnetic moments which surround a Sn site.

Combined magnetic and quadrupole interactions

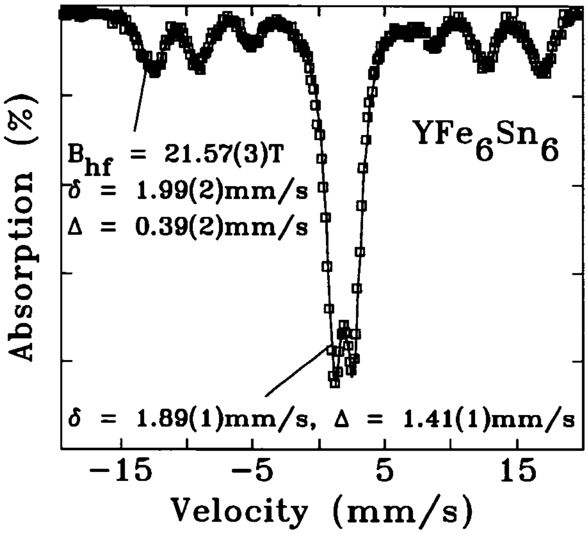

Figure 2.8: ^{119}Sn Mössbauer spectrum of $\mathrm{YFe_6Sn_6}$, which combines chemical isomer shift, quadrupole splitting and hyperfine field parameters.

In the $\mathrm{RMn_6Sn_6}$ compounds, both the quadrupole splitting and hyperfine field are present, in most cases at all three Sn sites. Figure 2.8 shows the variation in the appearance of ^{119}Sn Mössbauer patterns resulting from different Sn environments in YFe_6Sn_6 [6].

Mössbauer spectroscopy and spin reorientation

The Mössbauer parameters can be used to characterize the spin reorientation in the RMn_6Sn_6 systems, but a reference frame must first be identified. In a powder sample, the electric field gradient serves as a crystallographic reference frame. The high point symmetries of the three Sn sites in RMn_6Sn_6 ($6mm$ for Sn$-2e$ and $\overline{6}m2$ for Sn$-2c$ and Sn$-2d$) cause the crystallographic and electric field gradient axes to coincide, guaranteeing that the principal axis of the electric field gradient tensor V_{zz} lies along a, b or c. The local hexagonal point symmetries also impose axial symmetry ($\eta = 0$), such that the quadrupole splitting Δ is:

$$\Delta = \frac{eQV_{zz}}{4}(3cos^2\theta - 1) \tag{2.19}$$

where θ is the angle between V_{zz} and B_{hf} at the Sn site due to the surrounding magnetic moments. For $\theta = 90°$, $\Delta = -\frac{1}{4}eQV_{zz}$ and for $\theta = 0°$, $\Delta = \frac{1}{2}eQV_{zz}$, so that change in Δ by a factor of -2 corresponds to a change in moment direction by 90°.

Another of the Mössbauer parameters that can be used to identify the spin reorientation is R. The intensity of the second and fifth Mössbauer lines depends on the orientation of the magnetic moments with respect to the γ-ray (ϑ). Writing the intensity ratio as 3:R:1:1:R:3 for a six line Mössbauer pattern, ϑ can be determined:

$$R = \frac{4sin^2\vartheta}{1 + cos^2\vartheta} \tag{2.20}$$

For a single crystal, the moments point along a well defined direction with respect to the γ-direction. For example, the $TbMn_6Sn_{5.46}In_{0.54}$ single crystal platelets are grown with c perpendicular to the plane of the plates, parallel to γ. If the moments lie along the $c-$axis, then $\gamma \parallel c \parallel \mu$, giving $\vartheta = 0°$ and $R = 0$. If the moments are in the $ab-$plane, then $\gamma \parallel c \perp \mu$, giving $\vartheta = 90°$ and $R = 4$. Thus for an oriented sample, R can be used to determine the moment direction. For a powdered sample, R averages to 2 and this information is lost.

Calibration, magnetometry, refrigeration and external fields

In addition to the ^{119}Sn source described previously, a second source was used in this study for the purpose of calibration. The calibration of the spectrometer is a necessary and first step to a Mössbauer experiment because it will determine the true positions of all resonance lines as well as help identify possible equipment malfunctions. A 100 mCi Rh ^{57}Co source was used in conjunction with an α−Fe foil for the calibration of the spectrometer. This is a common choice, because the metallic iron spectrum has six hyperfine components which give a linearity check as well as defining a zero [41]. The six line Fe pattern (B_{hf} = 33 T, $R \sim 2$ and $\delta = -0.09(1)$ mm/s) was fitted as a reference for all successive isomer shift and hyperfine field measurements, and the room temperature spectrum is shown in Figure 2.9.

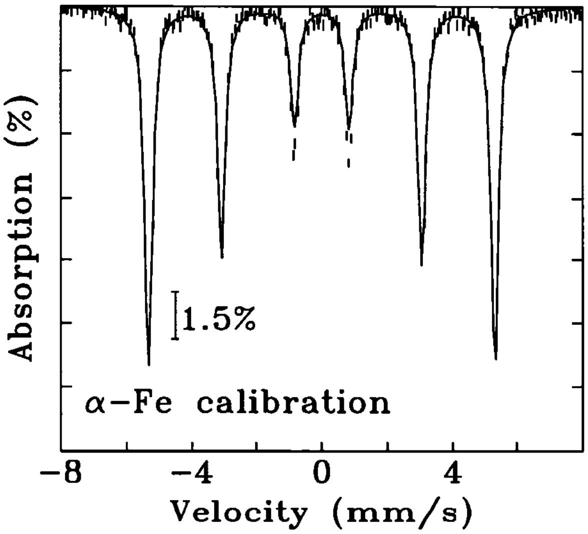

Figure 2.9: α-Fe calibration with a maximum velocity of 8 mm/s.

Basic magnetic characterization was carried out on a Quantum Design PPMS 9 T susceptometer/magnetometer. For the $RMn_6Sn_{6-x}Ga_x$ (R = Tb, Er) samples, the temperature was varied from 12 K to 300 K using a vibration-isolated closed-cycle refrigerator (Figure 2.10). The $TbMn_6Sn_{5.46}In_{0.54}$ mosaïc (Figure 2.1, right) was subject to external magnetic fields from 0 T to 1.53 T. The field was varied in a conventional electromagnet with the field perpendicular to both the γ-ray beam and the $c-$axis of the platelets. Finally, Mössbauer spectra were fitted using a conventional non-linear least-squares minimization routine. The routine uses a sum of Lorentzian lineshapes, and the line positions are calculated as a first order perturbation because the hyperfine fields in the Sn alloys are much larger than the quadrupole splittings. In cases where the two values are similar, this approach is not as accurate and the full Hamiltonian solution is required [31].

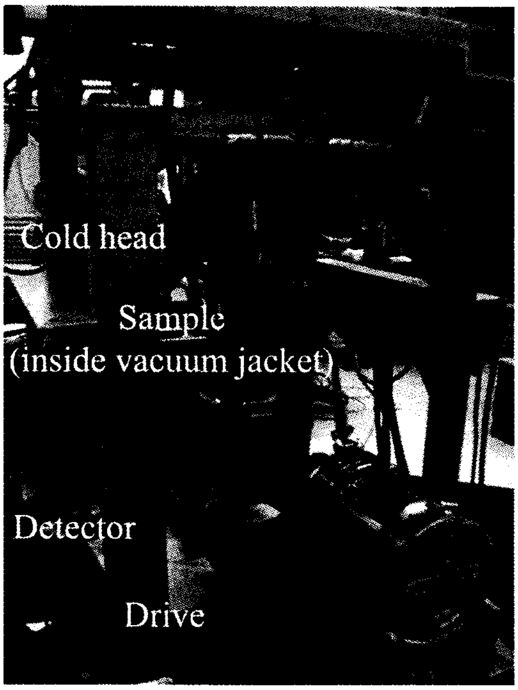

Figure 2.10: Vibration-isolated closed-cycle refrigerator, used to produce temperatures between 12 K and 300 K for the $TbMn_6Sn_{6-x}Ga_x$ samples.

Chapter 3

Spin reorientation in $ErMn_6Sn_{5.89}Ga_{0.11}$

In Chapter 1, the magnetic moments in RMn_6Sn_6 were shown to undergo a spontaneous temperature-induced spin reorientation from the $ab-$plane to the $c-$axis on cooling through T_{sr}. In the Tb compound, this occurs at a rather high temperature, $T_{sr} = 330$ K. At high temperatures, the Mössbauer lines overlap significantly. Isolating the spin reorientation from background temperature dependence of the moments is challenging.

Also, the temperature dependence of the moments is stronger at high temperatures, so that isolating the thermal changes in the moments due to the spin reorientation is a challenge. The same transition takes place in the ternary RMn_6Sn_6 compounds for R = Dy and Ho, but in both cases the reorientation is incomplete [5]. For the Er compounds, a small amount of Ga substitution at the Sn sites induces a spin reorientation below 100 K, as shown by Yao et al. [41]. We present here the evolution of the hyperfine parameters in the $ErMn_6Sn_{5.89}Ga_{0.11}$ compound.

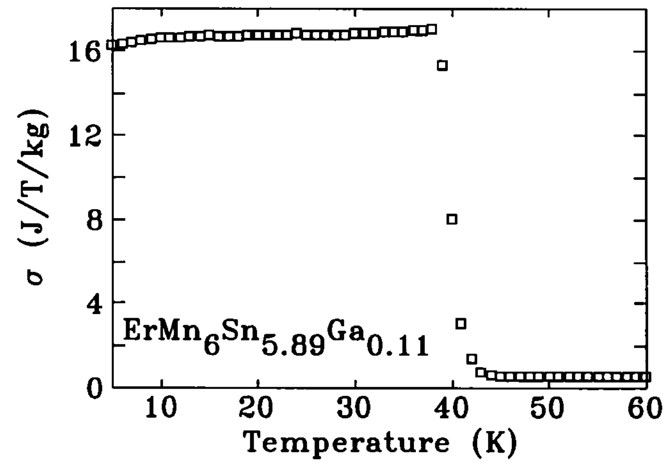

Figure 3.1: Magnetization of $ErMn_6Sn_{5.89}Ga_{0.11}$ in an applied field of 1 T, parallel to the c−axis.

3.1 Magnetometry

The Mn sublattice of the ternary $ErMn_6Sn_6$ compound orders antiferromagnetically at T_N = 352 K [7] (the Er sublattice remains paramagnetic), and the compound orders ferrimagnetically at 75 K. With a small amount of Ga substitution, the $ErMn_6Sn_{5.89}Ga_{0.11}$ compound is ferrimagnetic in its whole ordered range below the Néel point T_N = 372 K (for the In-substituted compound, the critical In concentration above which this occurs is $x_{in} = 0.2$). The thermomagnetic curves for an applied field of B_o = 1 T parallel to the c−axis are shown in Figure 3.1, for 2 K < T < 60 K. The anomaly at T_{sr} = 35(2) K marks the spin reorientation transition. This temperature is in fair agreement with that measured in the polycrystalline $ErMn_6Sn_{5.8}Ga_{0.2}$ compound (T_{sr} = 36 K) [41].

Figure 3.2 shows the thermomagnetic curves for B_o both along and perpendicular to the c−axis, and for 2 K < T < 450 K. An additional anomaly appears between 170 K and 225 K: the magnetization decreases but only when the applied field is perpendicular to the c−axis. This cannot be in response to a spin reorientation because the spin reorientation at 35(2) K is observed for both $B_o \perp c$ and for $B_o \parallel c$ (Figure 3.2). The decrease in magnetization is instead related to re-entrant ferrimagnetism, discussed in Section 1.6, and the stabilization of a helimagnetic structure in a narrow and intermediate temperature range [22]. The increasing antiferromagnetic character of the Mn sublattice upon cooling indicates that the Mn moments in the Mn–Er–Mn slab prefer to be antiparallel. On the other hand, the Er–Mn interactions are growing stronger with decreasing temperatures, favouring an antiparallel alignment of the rare earth and Mn sublattices, and forcing all of the Mn moments to be parallel. The competition between the two effects is the origin of re-entrant ferrimagnetism. The persistence of spontaneous magnetization in the present case indicates that the ferrimagnetic to helimagnetic transition is not complete. The ferrimagnetic arrangement is most likely partly broken in this temperature range (170 K to 225 K), resulting in a canted or conical structure (Figure 3.3).

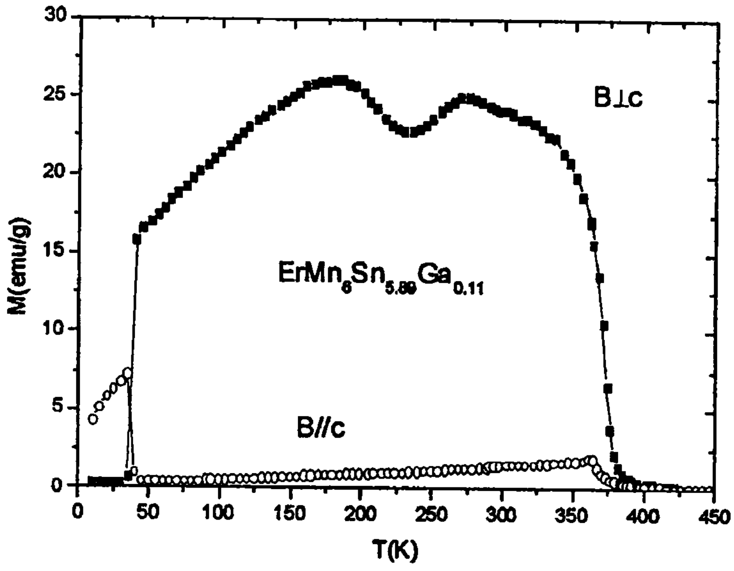

Figure 3.2: Magnetization of $ErMn_6Sn_{5.89}Ga_{0.11}$ in an applied field of 1 T, both parallel and perpendicular to c, for 2 K < T < 450 K [25].

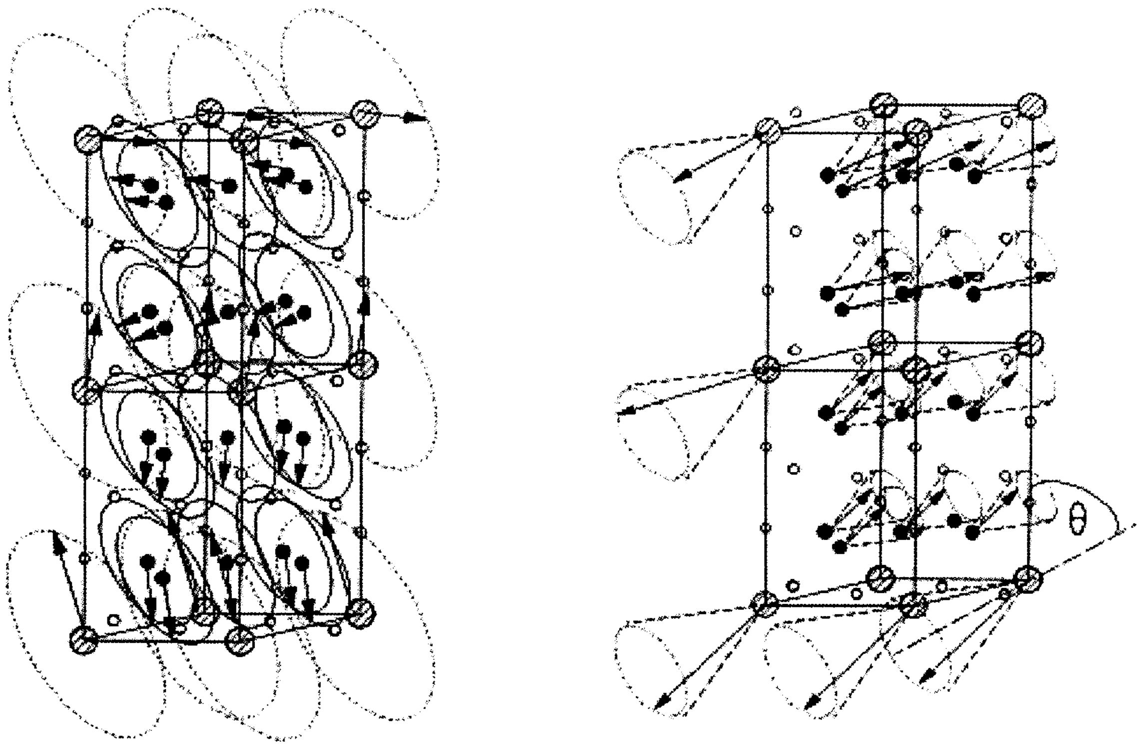

Figure 3.3: Left: helimagnetic structure of ternary (Er,Tm)Mn_6Sn_6. Right: canted or conical arrangement of the magnetic moments in $ErMn_6Sn_{5.89}Ga_{0.11}$, resulting from an incomplete transition from ferrimagnetism to helimagnetism in response to Ga doping [24].

3.2 Mössbauer spectroscopy

The 12 K Mössbauer pattern of $ErMn_6Sn_{5.89}Ga_{0.11}$ powder is shown in Figure 3.4. At 12 K, the pattern shows relatively distinguishable lines and was fitted with three subspectra, one for each Sn site, and a central impurity (spectral area 2.4%, and isomer shift $\delta = 2.72(6)$ mm/s relative to $\alpha-$Fe). The fits were designed to permit the areas of the three sextets to be adjusted freely. The Mössbauer parameters given by Mazet et al. [42] for $TbMn_6Sn_6$ at 4.2 K served as a guide to estimating the quadrupole splittings of the 12 K pattern. The uniqueness of the hyperfine parameters given by the fit allows for the unambiguous assignment of each of the three Mössbauer sextets to a specific Sn site.

The three subspectra at 12 K have quadrupole splittings $\Delta = 1.55(2)$ mm/s,

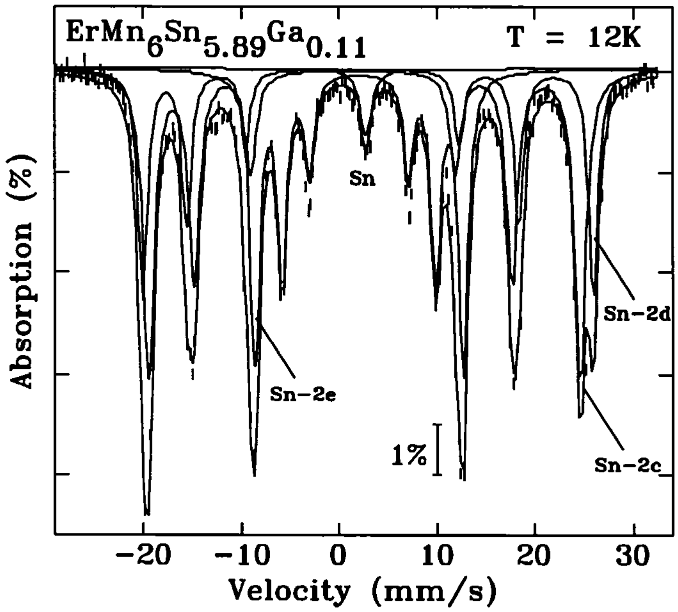

Figure 3.4: Mössbauer spectrum for $ErMn_6Sn_{5.89}Ga_{0.11}$ at 12 K.

1.17(2) mm/s and 0.03(2) mm/s and hyperfine fields B_{hf} = 33.56(2) T, 32.12(2) T and 15.54(2) T respectively. The site assignments are based on previous studies of $HfMn_6Sn_6$ at 100 K, whose crystal structure is identical to that of $ErMn_6Sn_{5.89}Ga_{0.11}$ but with antiferromagnetic order [1]. The arrangement of magnetic moments around the Sn−2*c* site in $HfMn_6Sn_6$ is such that there is no net transferred hyperfine field (Figure 1.3 in Section 1.4). The quadrupole splitting at Sn−2*c* in $HfMn_6Sn_6$ is measured to be Δ = 1.1 mm/s, and assuming the replacement of non-magnetic Hf with magnetic Er has little or no effect on the crystalline electric field, we can assign the Δ = 1.17(2) mm/s sextet in $ErMn_6Sn_{5.89}Ga_{0.11}$ to the Sn−2*c* site. The hyperfine field of 32.12(2) T is entirely due to the trigonal Er plane which surrounds Sn−2*c*. We can attribute the slightly larger Δ = 1.55(2) mm/s (B_{hf} = 33.56(2) T) to the geometrically similar Sn−2*d* (in $HfMn_6Sn_6$, Δ = 1.6 mm/s at Sn−2*d*). It is not surprising that the quadrupole splittings and hyperfine fields at the Sn−2*c* and Sn−2*d* sites are close, because the only difference between the two sites is a plane of Er atoms surrounding Sn−2*c* (the bond lengths are 2.74 Å and 2.78 Å for Sn−2*c* and Sn−2*d*).

The remaining sextet ($\Delta = 0.03(2)$ mm/s and $B_{hf} = 15.54(2)$ T) is assigned to the Sn$-2e$ site ($\Delta = 0.02$ mm/s for Sn$-2e$ in HfMn$_6$Sn$_6$). This assignment is also a reasonable one because the quadrupole splitting and hyperfine field are much smaller than for the other Sn sites, owing to the drastically different Mn environment. The Sn$-2e$ site assignment will be confirmed in Chapter 6.

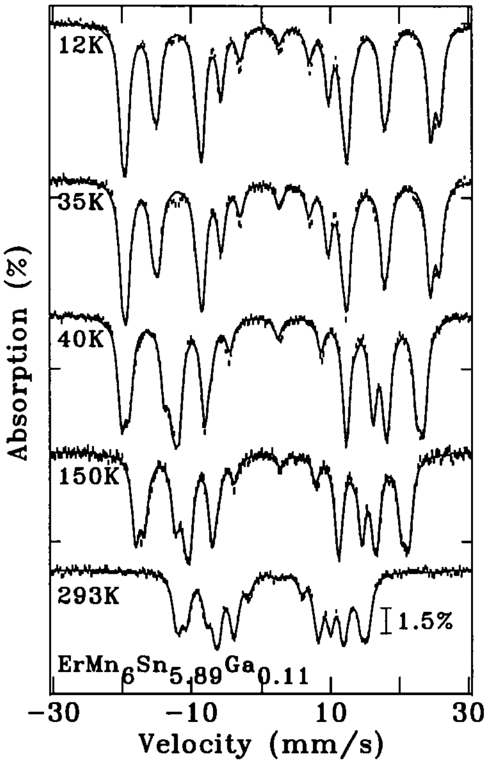

Figure 3.5: Mössbauer spectra of ErMn$_6$Sn$_{5.89}$Ga$_{0.11}$, from 12 K to 300 K. The spin reorientation transition occurs at $T_{sr} = 38(2)$ K.

The nature of the impurity phase ($\delta = 2.72(6)$ mm/s at 12 K) can be determined by heating the sample to room temperature from 12 K, and by determining the Debye temperature from the thermal evolution of the recoil free fraction (Chapter 2). The Mössbauer spectra from 12 K to 300 K are shown in Figure 3.5. The total absorption (normalized to the baseline) was plotted as a function of temperature and from this a Debye temperature of $\theta_D = 165(5)$ K was measured (Figure 3.6), as calculated in the high-temperature limit. The isomer shift and Debye temperature for β-Sn are

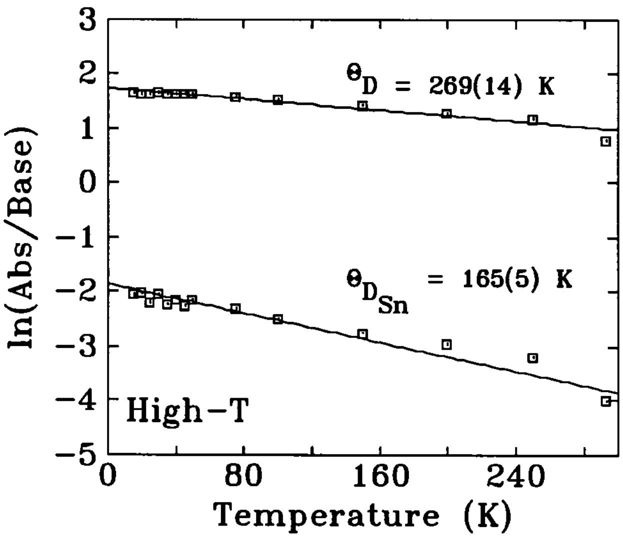

Figure 3.6: Natural log of the recoil-free fraction (total absorption divided by baseline) as a function of temperature, in the high-temperature limit (see Chapter 2). From the slope, the Debye temperature of $ErMn_6Sn_{5.89}Ga_{0.11}$ and the impurity phase ($\theta_{D_{Sn}}$) are measured.

δ =2.56 mm/s [35] and θ_D = 135 K [43], and those for SnO are δ =2.71 mm/s [44] and θ_D = 181(2) K [45]. Since the isomer shifts and Debye temperatures compare relatively well, the impurity phase in $ErMn_6Sn_{5.89}Ga_{0.11}$ is likely to be elemental Sn, SnO, or a mixture of both.

At 12 K, the Mössbauer lines are mostly distinct, but increasing temperature introduces dense overlapping of several of the Mössbauer lines, notably at $T > T_{sr}$. Thus the fitting of spectra for 12 K < T < 300 K involved a few carefully constructed constraints. The spin reorientation is expected to be a full 90° rotation of the moments, and since such a rotation corresponds to a change in quadrupole splitting by a factor of −2 (Section 2.2.4), we can estimate the quadrupole splittings for $T > T_{sr}$ based on those fitted at 12 K. The areas of the three Mössbauer sextets were constrained (allowing the central Sn impurity area to vary and eventually vanish) to the average values seen at $T \ll T_{sr}$, because as long as the three subspectra have the same recoil-free fraction and Debye temperature, the area ratio between them cannot change. This constraint allows for the quadrupole splittings and hyperfine fields (as

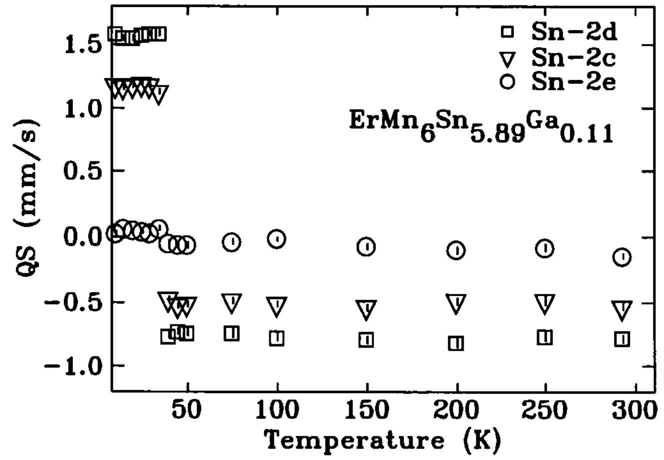

Figure 3.7: Quadrupole splittings of the three Sn sites in $ErMn_6Sn_{5.89}Ga_{0.11}$ between 12 K and 300 K.

well as the isomer shifts) to be adjusted freely, provided all of these parameters are well behaved.

The spin reorientation transition is characterized by a drastic change in appearance of the spectra between 35 K and 40 K. Figure 3.7 shows the quadrupole splittings of the three Sn sites as functions of temperature. The factor of −2 change in quadrupole splitting on cooling through 38(2) K marks the spin reorientation (Table 3.1). As discussed in Section 2.2.4 of Chapter 2, this corresponds to a rotation of the moments by 90° at $T_{sr} = 38(2)$ K, from the *ab*−plane for $T > T_{sr}$ to the *c*−axis for $T < T_{sr}$. The width of the transition is less than 5 K, so the reorientation is an abrupt, well-defined transition.

	$T < T_{sr}$ ($\mu \parallel c$) 35 K		$T > T_{sr}$ ($\mu \perp c$) 40 K	
Site	Δ (mm/s)	B_{hf} (T)	Δ (mm/s)	B_{hf} (T)
Sn−2*c*	1.11(2)	31.99(2)	−0.51(2)	31.87(2)
Sn−2*d*	1.54(3)	33.46(3)	−0.81(3)	30.33(2)
Sn−2*e*	0.07(2)	15.45(2)	−0.03(2)	20.53(2)

Table 3.1: Mössbauer parameters at 35 K and 40 K in $ErMn_6Sn_{5.89}Ga_{0.11}$.

The temperature dependence of the hyperfine fields at the three Sn sites is shown in Figure 3.8. In the discussion above, the assignment of each subspectrum to a Sn site was based on the electrostatic environment (quadrupole splitting) at each Sn site. This assignment cannot be based on the magnetic neighbours of the Sn sites because, as shown in Figure 3.8, two of the hyperfine fields (Sn$-2c$ and Sn$-2d$) exchange sequence at the reorientation. For instance, if the largest field were to be associated with the site having the most magnetic neighbours (in this case Sn$-2c$ for T > T_{sr}), the assignment would be different depending on whether the measurement were made above or below T_{sr}. Instead, the site assignment was based on the quadrupole splitting, because the projection of the electric field gradient tensor changes by the same factor for all sites when the moments rotate.

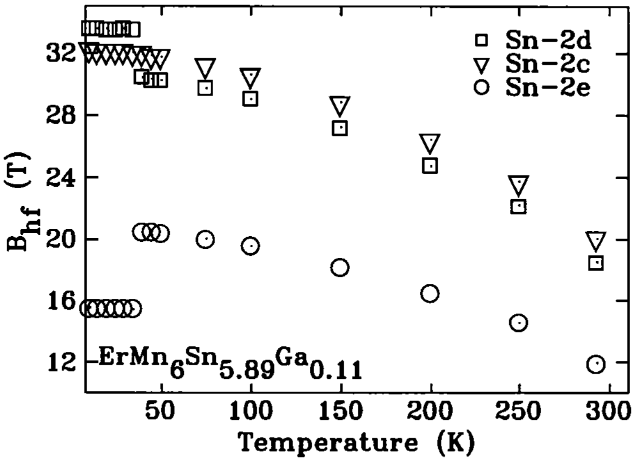

Figure 3.8: Hyperfine fields ar the three Sn sites in $ErMn_6Sn_{5.89}Ga_{0.11}$ (12 K < T < 300 K).

The hyperfine fields at the three Sn sites each behave differently through the reorientation (Figure 3.8). On cooling through T_{sr}, B_{hf} decreases dramatically at Sn$-2e$, increases substantially at Sn$-2d$, and increases only very slightly at Sn$-2c$. In Chapter 1, it was shown that the spin reorientation affects only the anisotropic contribution to the hyperfine field. Therefore, in order to determine the anisotropic contribution, it is necessary to quantify the changes in B_{hf} due to the reorientation. The temperature dependence of B_{hf} was fitted to two Brillouin functions: one for T

$< T_{sr}$ and another for $T > T_{sr}$. Each of the Brillouin curves was extrapolated to T_{sr} to give the fractional change in hyperfine field,

$$\Delta B_{hf} = \frac{\delta B_{hf}}{B_{hf}^{sr}} \tag{3.1}$$

where δB_{hf} is the difference and B_{hf}^{sr} is the hyperfine field at T_{sr} for $\mu \parallel c$. As reflected in the plot of hyperfine fields, this fractional change differs significantly for each site (Table 3.2). Chapter 6 gives a full discussion on the calculation of the anisotropic contribution to the hyperfine field using δB_{hf} and B_{hf}^{sr}.

Site	δB_{hf} (T)	ΔB_{hf}
Sn−2*c*	0.4(2)	0.011(4)
Sn−2*d*	3.3(2)	0.100(6)
Sn−2*e*	−4.9(1)	−0.314(6)

Table 3.2: The two $T < T_{sr}$ and $T > T_{sr}$ Brillouin curves are extrapolated to $T = 0$ K in ErMn$_6$Sn$_{5.89}$Ga$_{0.11}$. The difference δB_{hf} is normalized to the 0 K B_{hf} with $\mu \parallel c$ to give the fractional change ΔB_{hf}.

In ErMn$_6$Sn$_6$, the Mn sublattice orders antiferromagnetically at 352 K , whereas the Er sublattice orders ferromagnetically at 75 K [13], at which point the structure undergoes an antiferromagnetic to ferrimagnetic transition. This transition does not however imply a spin reorientation, because the second order crystal field parameters (B_2^0) of both sublattices are both positive. The easy plane anisotropy in ErMn$_6$Sn$_6$ has been shown to be relatively weak [25]. Since a small amount of Ga doping results in a spin reorientation from the *ab*−plane to the *c*−axis, this indicates that the Ga substitution has changed the Er anisotropy from easy plane (*ab*) to easy axis (*c*) [46].

Chapter 4

Spin reorientation in $TbMn_6Sn_{6-x}Ga_x$

In the previous section, it was shown how a low level of Ga doping in $ErMn_6Sn_{6-x}Ga_x$ sufficed to induce a spin reorientation below 100 K. We now wish to examine doping effects on spin reorientation in RMn_6Sn_6, but two main issues arise for the $ErMn_6Sn_{6-x}Ga_x$ compounds: their magnetic structures are complicated, and they must be doped with Ga or In in order to undergo a spin reorientation transition. It is thus simpler to choose a rare earth compound which has an easy axis anisotropy to compete with the planar Mn anisotropy, so that the spin reorientation occurs without doping and is a much cleaner transition. The moments in ternary $TbMn_6Sn_6$ undergo a 90° spin reorientation at $T_{sr} = 330$ K (Section 1.2.2), and doping in $TbMn_6Sn_{6-x}Ga_x$ allows the easy plane anisotropy of the Mn sublattice to dominate over wider temperature ranges. As a result, the substitution drives T_{sr} down to a more convenient temperature range. Here, the effect of Ga substitution on the spin reorientation temperature in $TbMn_6Sn_{6-x}Ga_x$ ($0.2 \leq x \leq 0.8$) is discussed.

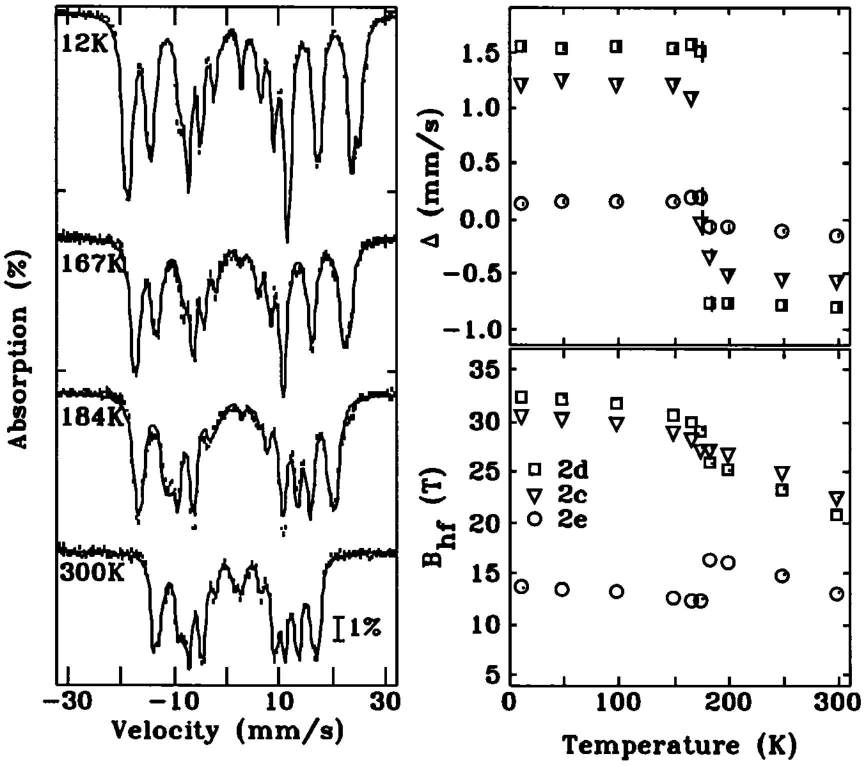

Figure 4.1: Left: ^{119}Sn Mössbauer spectra of $TbMn_6Sn_{5.4}Ga_{0.6}$ from 12 K to 300 K. Right: quadrupole splitting (top) and hyperfine field (bottom) at the three Sn sites in $TbMn_6Sn_{5.4}Ga_{0.6}$, as functions of temperature. The spin reorientation temperature (T_{sr}) is 180(5) K.

4.1 Mössbauer spectroscopy

Figure 4.1 (left) shows the Mössbauer spectra of $TbMn_6Sn_{5.4}Ga_{0.6}$ from 12 K to 300 K. They consist of three subspectra (one for each Sn site) and a central Sn impurity. The areas of the three Mössbauer sextets were constrained to the average values seen for $T \ll T_{sr}$. The assignment of subspectra to Sn sites was not only based on the Mössbauer parameters of $HfMn_6Sn_6$, as in the previous chapter, but also on the similarities between the two $RMn_6Sn_{6-x}Ga_x$ (R = Er, Tb) compounds. Table 4.1 lists the parameters at 12 K for the $x = 0.2$ and $ErMn_6Sn_{5.89}Ga_{0.11}$ compounds. The comparison is made at 12 K where the Mössbauer lines are more distinguishable and where the moments are parallel to the c−axis.

The x-ray single crystal refinement and neutron diffraction study of $RMn_6Sn_{6-x}Ga_x$

T = 12 K	$ErMn_6Sn_{5.89}Ga_{0.11}$ ($\mu \parallel c$)		$TbMn_6Sn_{5.8}Ga_{0.2}$ ($\mu \parallel c$)	
Site	Δ (mm/s)	B_{hf} (T)	Δ (mm/s)	B_{hf} (T)
Sn−2*c*	1.00(2)	32.12(2)	1.11(1)	30.44(4)
Sn−2*d*	1.50(3)	33.56(2)	1.57(3)	32.94(4)
Sn−2*e*	0.00(2)	15.54(2)	0.16(1)	13.81(2)

Table 4.1: Mössbauer parameters at 12 K in $ErMn_6Sn_{5.89}Ga_{0.11}$ and $TbMn_6Sn_{5.8}Ga_{0.2}$. The comparison of parameters between the two similar compounds guided the site assignment in $TbMn_6Sn_{5.8}Ga_{0.2}$ (and subsequently the other three $TbMn_6Sn_{6-x}Ga_x$ compounds).

(R = Tm, Tb; x = 1.2-2.6) [23][24][12] showed that Ga substitution occurs at both the Sn−2*c* and Sn−2*d* sites, with a distinct preference for Sn−2*c*, while mostly avoiding Sn−2*e*. The present Mössbauer study of the $TbMn_6Sn_{6-x}Ga_x$ compounds in contrast shows this substitution to occur mostly on Sn−2*d*. The area of the Mössbauer subspectrum associated with the Sn−2*d* site shows a strong dependence on Ga concentration. The systematic reduction of the area of the Sn−2*d* component with increasing x indicates the de-population of Sn atoms at the Sn−2*d* site caused by their replacement by Ga atoms (Figure 4.2). There is also evidence for a slight bias for the Sn−2*e* site. After renormalizing to the Sn−2*c* area, the Sn−2*e* areas show a weak dependence on the level of Ga doping and decrease with x in the same manner as Sn−2*d*, though the effect is much smaller. It should also be noted that a different site preference was reported for In-substituted compounds [47], for which the In atoms prefer the Sn−2*d* site.

In Chapter 2, it was shown that a comparison of the Debye temperatures of the three Sn sites can be used to confirm that a reduction in spectral areas is not an effect of reduced recoil-free fractions. Figure 4.3 shows the temperature dependence of the total absorption for the three Sn sites, and the resulting Debye temperatures (for the high-temperature limit). Since the three θ_D values are within error, the reduced spectral area at Sn−2*d* and Sn−2*e* discussed above is indeed a result of reduced Sn occupancies.

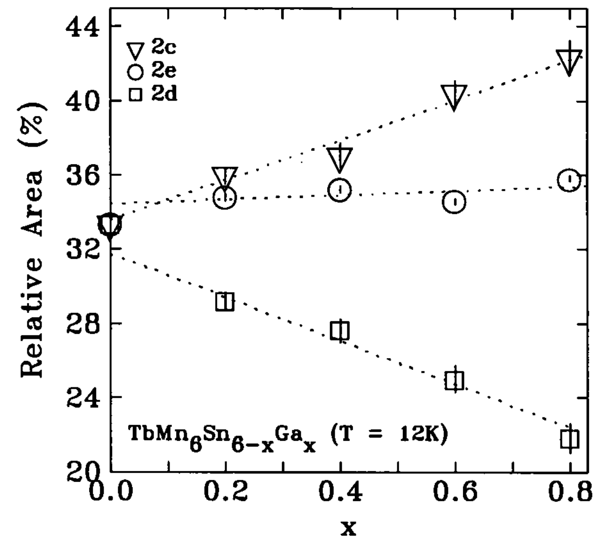

Figure 4.2: Relative areas of the three Sn sites with x, measured at 12 K.

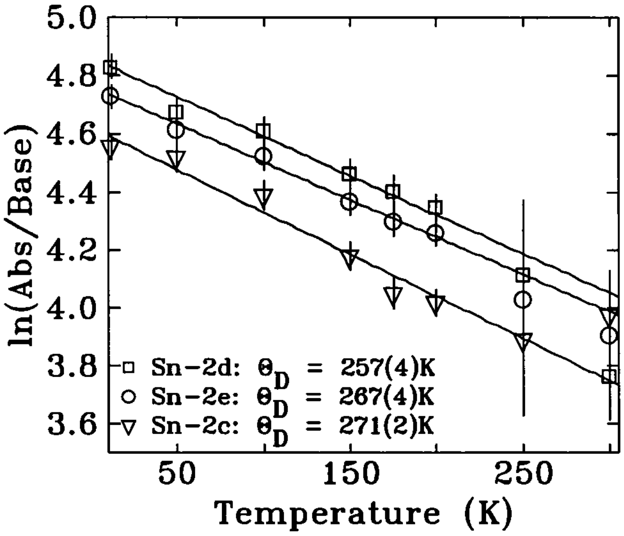

Figure 4.3: Debye temperature of the three Sn sites in TbMn$_6$Sn$_{5.6}$Ga$_{0.4}$. They are near to within error of one another, indicating that the reduction in spectral areas shown in Figure 4.2 is not an effect of reduced recoil-free fractions.

Figure 4.1 (top, right) shows the temperature dependence of the quadrupole splittings at the three Sn sites in TbMn$_6$Sn$_{5.4}$Ga$_{0.6}$. On cooling through T$_{sr}$ = 180(5) K, Δ changes by a factor of -2, as seen in the previous chapter. This again corresponds to a change in moment direction of 90° from the ab–plane for $T > T_{sr}$ to the c–axis

	$T < T_{sr}$ ($\mu \parallel c$) 167 K		$T > T_{sr}$ ($\mu \perp c$) 200 K	
Site	Δ (mm/s)	B_{hf} (T)	Δ (mm/s)	B_{hf} (T)
Sn−2*c*	1.11(3)	28.40(3)	−0.51(3)	26.73(3)
Sn−2*d*	1.56(4)	29.91(4)	−0.77(5)	25.18(5)
Sn−2*e*	0.21(3)	12.39(3)	−0.07(3)	16.20(2)

Table 4.2: Mössbauer parameters at 167 K and 200 K in $TbMn_6Sn_{5.4}Ga_{0.6}$.

for $T < T_{sr}$. The change by a factor of −2 in the quadrupole splitting is consistent throughout the entire range of Ga composition. Table 4.2 shows the hyperfine parameters in $TbMn_6Sn_{5.4}Ga_{0.6}$ for $T < T_{sr}$ and $T > T_{sr}$.

The hyperfine fields at the three Sn sites in $TbMn_6Sn_{5.4}Ga_{0.6}$ are plotted with temperature in Figure 4.1 (bottom, right). On cooling through T_{sr}, B_{hf} increases at Sn−2*d* and decreases at Sn−2*e*, and both are dramatic effects. In contrast, the hyperfine field at Sn−2*c* increases only slightly through the reorientation. These observations are identical to the behaviour seen in Section 3.2 of Chapter 3 for the $ErMn_6Sn_{5.89}Ga_{0.11}$ compound. The fractional change in hyperfine field ΔB_{hf} for each Sn site (obtained by fitting each temperature dependence to two Brillouin curves, as described in the previous chapter) is plotted as a function of composition in Figure 4.4. There is evidence for a slight increase in $|\Delta B_{hf}|$ for increasing Ga content, x.

The spin reorientation temperature (T_{sr}) is a strong function of Ga content (x), showing a significant decrease of 255 ± 18 K/Ga as x increases from 0.2 to 0.8 (Figure 4.5). The extrapolated reorientation temperature for $x = 0$ is $T_{sr} = 330(19)$ K, in excellent agreement with the 330 K given by Venturini et al. [7]. This variation in T_{sr} is an effect of the electron density at the Sn site, and a different choice of substituting atom renders a different spin reorientation temperature as a well as a different trend with respect to composition. Lefèvre et al. [19] have shown that the spin reorientation temperature of the $(Tb,Dy)Mn_6Sn_{6-x}In_x$ series shows no distinct relation to In concentration ($0.2 \leq x \leq 0.8$). The example shown in Figure 4.5 is

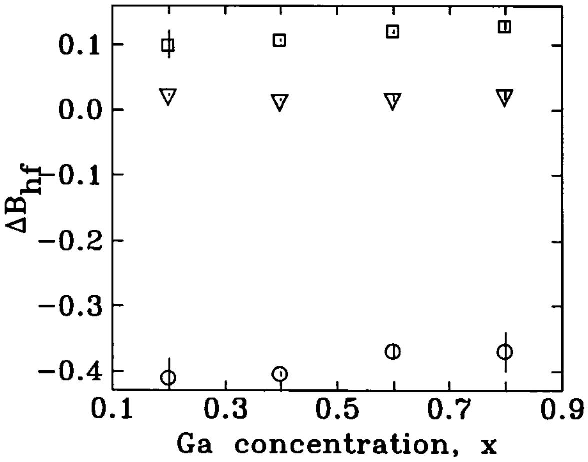

Figure 4.4: Fractional change in B$_{hf}$ extrapolated to T$_{sr}$ on two Brillouin curves, for T < T$_{sr}$ and T > T$_{sr}$, obtained by normalizing the difference δ to the B$^{sr}_{hf}$ with $\mu \parallel c$.

for TbMn$_6$Sn$_{6-x}$In$_x$. This could indicate that the substitution of In for Sn does not significantly alter the magnetocrystalline anisotropy of the rare earth and Mn sublattices. As T$_{sr}$ strongly depends on Ga content in TbMn$_6$Sn$_{6-x}$Ga$_x$, this substitution most likely has a greater effect on the magnetocrystalline anisotropy of the sublattices than In substitution. There is an observed critical Ga concentration ($x_{crit} \geq$ 1.0) above which this argument is no longer valid [19]. For instance, in TbMn$_6$Sn$_5$Ga, no spin reorientation occurs at all [12], as the planar anisotropy of the Mn sublattice dominates in the whole ordered range.

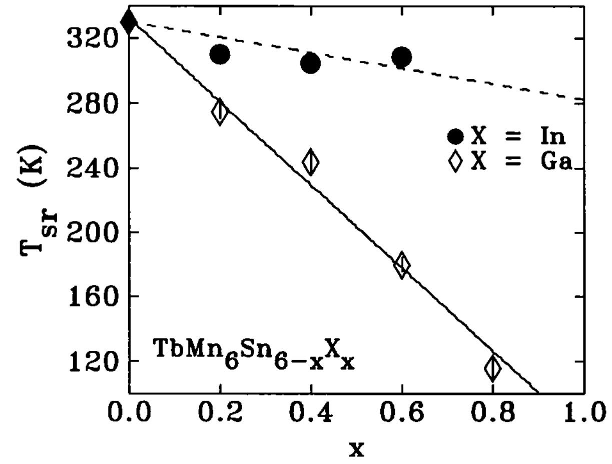

Figure 4.5: Effect of doping on T_{sr} in $TbMn_6Sn_{6-x}X_x$ compounds. For X = Ga, T_{sr} decreases by 255±18 K/Ga, from 330 K at $x = 0$ (filled diamond) to 116(8) K at $x = 0.8$. For X = In, the T_{sr} dependence on x is much weaker (In results from [19]).

Chapter 5

Spin-flop in $TbMn_6Sn_{5.46}In_{0.54}$

In the previous chapters, the temperature-induced spin reorientation in powdered samples of $RMn_6Sn_{6-x}Ga_x$ (R = Er, Tb) was discussed. Recall that spin reorientation can also be field-induced, if the applied magnetic field is large enough to force the moments to rotate. As the moment direction in a powder is random, it is easiest to observe the spin-flop in oriented single crystals. In a single crystal, the orientation of the magnetic moments can be determined through the intensity ratio, R (see Chapter 2). The in-field Mössbauer study of an oriented RMn_6Sn_6 single crystal thus provides additional information regarding the moment direction, because the moment orientation before and after the spin-flop can be explicitly determined. It is possible to grow very thin single crystal platelets of $TbMn_6Sn_{6-x}In_x$ which are suitable for Mössbauer spectroscopy, and we show here the study of spin-flop in this compound (with $x = 0.54$).

5.1 Magnetometry

The thermal variation of the magnetization of the single crystals measured above room temperature indicate the Néel point to be $T_N = 397(3)$ K for $TbMn_6Sn_{5.46}In_{0.54}$ [48]. In addition, the compound displays a spin reorientation transition at $T_{sr} = 317(3)$ K

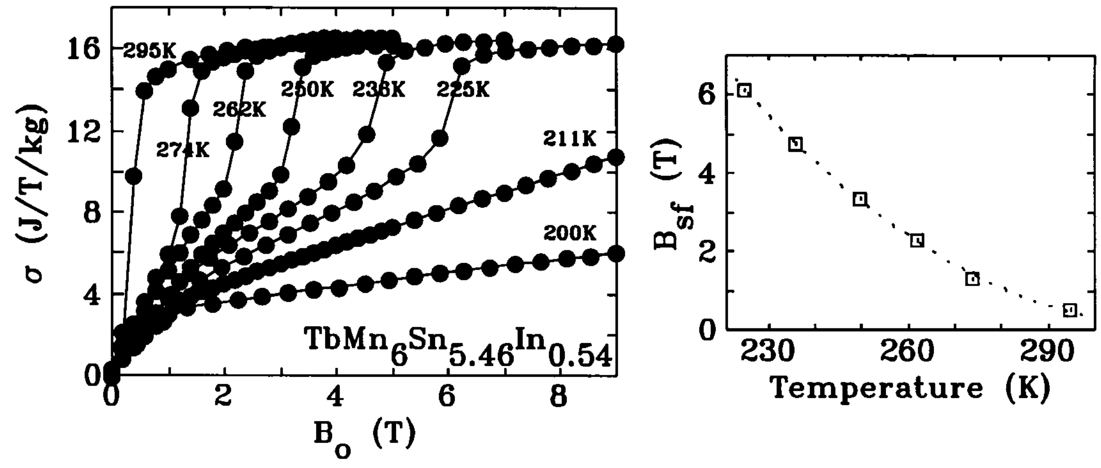

Figure 5.1: Left: Magnetization of $TbMn_6Sn_{5.46}In_{0.54}$ in an applied field range of 0 T to 9 T and for T < T_{sr}. The applied field is perpendicular to the c–axis. Right: Temperature dependence of the spin-flop field in $TbMn_6Sn_{5.46}In_{0.54}$ for T < T_{sr}. The dotted line is a guide to the eye.

characterized by a change of the easy direction from the ab–plane at high temperature (T > T_{sr}) to the c–axis for $T < T_{sr}$.

Figure 5.1 (left) shows the magnetization of a $TbMn_6Sn_{5.46}In_{0.54}$ single crystal as a function of applied field, where B_o is perpendicular to c, and T < T_{sr}. In an applied field of ~0.5 T at room temperature, a spin-flop is induced to the direction along which B_o is applied (ab–plane). This confirms the moments are along the c–axis at room temperature. The spin-flop field increases with decreasing temperature (Figure 5.1, right). As the spin-flop field is expected to exceed the available 9 T by 220 K, the spin-flop is unattainable for 211 K and below.

5.2 Mössbauer spectroscopy

Figure 5.2 (left) shows the Mössbauer spectra for $TbMn_6Sn_{5.46}In_{0.54}$ in applied fields ranging from 0 T to 1.53 T. In order to assign the subspectra to Sn sites as seen in Sections 3.2 and 4.1, the sample was cooled to 12 K where the Mössbauer lines are more distinguishable. The site assignments at 12 K followed those of the $RMn_6Sn_{6-x}Ga_x$ cases (R = Er, Tb) and sample parameters are shown in Table 5.1. At 300 K, the

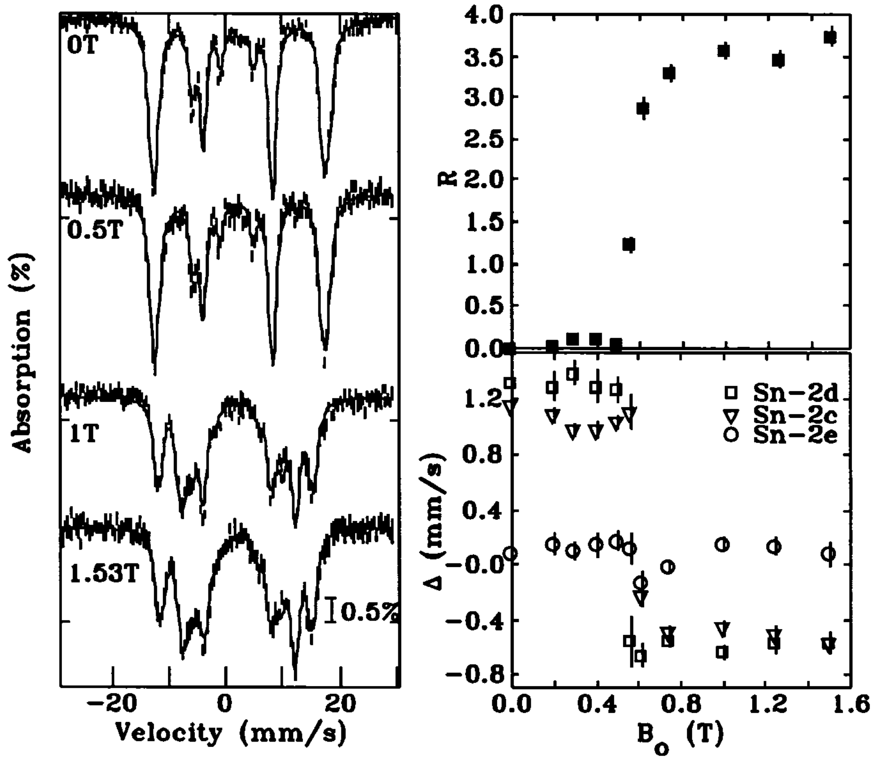

Figure 5.2: Left: ^{119}Sn Mössbauer spectra of $TbMn_6Sn_{5.46}In_{0.54}$ from 0 T to 1.53 T. Right: R ratio (top) and quadrupole splitting (bottom) of the three Sn sites as functions of applied field. The spin-flop occurs at $B_{sf} = 0.57(3)$ T.

quadrupole splittings were set to those determined at 12 K and the fields and isomer shifts were adjusted freely. The area constraint was 1:1:1.

For the single crystal platelets of $TbMn_6Sn_{5.46}In_{0.54}$, the moments are oriented along a unique direction with respect to the γ propagation direction. Through magnetometry it was shown that at 295 K and below, the moments are along the $c-$axis (parallel to γ). The intensity ratio R is plotted in Figure 5.2 (top right) as a function of applied field. For $B_o < B_{sf}$, $R = 0$ confirms that the moments are parallel to the γ-rays ($\vartheta = 0°$) and to c. Once the spin-flop has occurred, an abrupt change in R from 0 to 3.7(1) is observed, indicating a change in moment direction. R is not 4 as expected for a full rotation into the $ab-$plane. This is due either to an incomplete rotation of the moments or to saturation effects. However, the factor of -2 change

T = 12 K	$TbMn_6Sn_{5.4}Ga_{0.6}$ ($\mu \parallel c$)		$TbMn_6Sn_{5.46}In_{0.54}$ ($\mu \parallel c$)	
Site	Δ (mm/s)	B_{hf} (T)	Δ (mm/s)	B_{hf} (T)
Sn−2*c*	1.23(2)	30.57(2)	1.09(5)	26.26(2)
Sn−2*d*	1.55(3)	32.39(3)	1.33(9)	27.94(3)
Sn−2*e*	0.14(2)	13.64(2)	0.02(4)	12.23(2)

Table 5.1: Mössbauer parameters at 12 K in $TbMn_6Sn_{5.4}Ga_{0.6}$ and $TbMn_6Sn_{5.46}In_{0.54}$. The comparison of parameters between the two similar compounds guided the site assignment in $TbMn_6Sn_{5.46}In_{0.54}$.

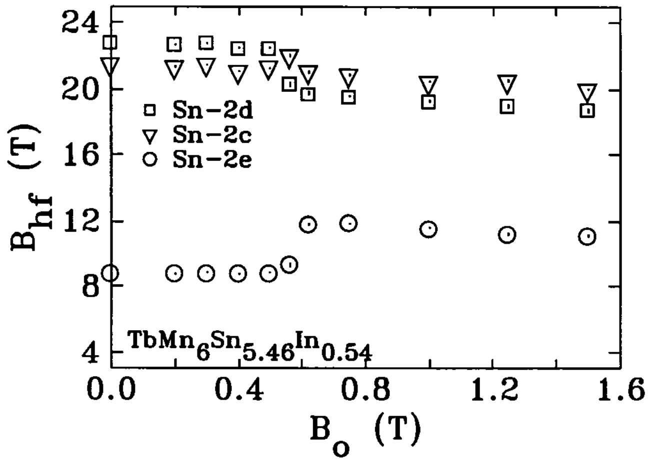

Figure 5.3: Hyperfine fields at the three Sn sites in $TbMn_6Sn_{5.46}In_{0.54}$. The reorientation of the moments at 0.57(3) T on increasing applied fields causes an increase in B_{hf} at Sn−2*e*, and a decrease in B_{hf} at Sn−2*c* and Sn−2*d*.

in quadrupole splitting (Figure 5.2, top right) associated with the spin-flop confirms that the rotation is complete. Therefore, the effect is likely due to the saturation of lines 2 and 5, caused by samples which are somewhat thick (the platelet thickness is ~60 μm).

Figure 5.3 shows the hyperfine fields at the three Sn sites as functions of applied field. For increasing B_o, the spin-flop is associated with an increase in B_{hf} at Sn−2*e*, and a decrease at Sn−2*c* and Sn−2*d*. These observations agree with those of the thermally-driven spin reorientation in $(Er,Tb)Mn_6Sn_{6-x}Ga_x$. The field dependence of B_{hf} was fitted to two lines of slope −1 (Section 2.2.4 of Chapter 2): one for $B_o < B_{sf}$

	T-induced				B_o-induced	
	$ErMn_6Sn_{5.89}Ga_{0.11}$		$TbMn_6Sn_{5.4}Ga_{0.6}$		$TbMn_6Sn_{5.46}In_{0.54}$	
Site	δB_{hf} (T)	ΔB_{hf}	δB_{hf} (T)	ΔB_{hf}	δB_{hf} (T)	ΔB_{hf}
Sn−2c	0.4(2)	0.011(4)	0.4(1)	0.016(5)	0.2(2)	0.01(1)
Sn−2d	3.3(2)	0.100(6)	2.9(1)	0.107(4)	2.39(5)	0.104(2)
Sn−2e	−4.9(1)	−0.314(6)	−4.5(1)	−0.40(2)	−4.1(1)	−0.45(3)

Table 5.2: In $ErMn_6Sn_{5.89}Ga_{0.11}$ and $TbMn_6Sn_{5.4}Ga_{0.6}$, the two $T < T_{sr}$ and $T > T_{sr}$ Brillouin curves are extrapolated to T_{sr}. The difference δB_{hf} is normalized to the B_{hf}^{sr} with $\mu \parallel c$ to give the fractional change ΔB_{hf}. In $TbMn_6Sn_{5.46}In_{0.54}$, the two $B_o < B_{sr}$ and $B_o > B_{sr}$ lines of slope -1 are extrapolated to 0 T. The difference δB_{hf} is normalized to the 0 T B_{hf} with $\mu \parallel c$, giving ΔB_{hf}.

and another for $B_o > B_{sf}$. The lines were extrapolated to 0 T to give the fractional change $\Delta B_{hf} = \delta B_{hf}/B_{hf}^0$ where δB_{hf} is the difference and B_{hf}^0 is the 0 T hyperfine field ($\mu \parallel c$). In Table 5.2, ΔB_{hf} is compared to that obtained in the thermally-driven cases. The close agreement between the three measurements of ΔB_{hf} demonstrates that the anisotropic contribution can be obtained through both temperature-induced and field-induced spin reorientation and that it is independent of the driving force. The fractional change in hyperfine field due to the anisotropic contribution is large and negative in the case of Sn−2e, and smaller and positive at the Sn−2c and Sn−2d sites.

Chapter 6

Discussion

In comparing the last three chapters, we notice that there are several similarities amongst the $\mathrm{RMn_6Sn_{6-x}X_x}$ (R = Er, Tb; X = Ga, In) systems:

- In both the temperature-induced and field-induced spin reorientations, the quadrupole splittings at all Sn sites change by a factor of -2 (on increasing temperature through T_{sr} or on increasing field through B_{sf}). This corresponds to a change in moment direction of 90°. As the moments lie along the c−axis for $\mathrm{T} < \mathrm{T}_{sr}$ or $\mathrm{B}_o < \mathrm{B}_{sf}$, they flop into the ab−plane at the reorientation temperature or field.

- There is a striking change in hyperfine field at two of the Sn sites, marked by a decrease at Sn−2d and an increase at Sn−2e (on increasing temperature or field through T_{sr} or B_{sf}), in response to the moment reorientation. The effect at Sn−2c is much smaller.

- The fractional change $\Delta\mathrm{B}_{hf}$ for each site observed at the reorientation is similar in all of the compounds investigated and is independent of the driving force of the reorientation (Table 5.2).

The last point is the focus of this section. Since the isotropic contribution to B_{hf} is independent of moment orientation, the changes in hyperfine field due to the rota-

State I (90 K)			State II (70 K)		
Site	B_{hf} (T)	θ	Site	B_{hf} (T)	θ
Sn1	6.6(2)	90°	Sn1′	20.6(2)	0°
Sn2	4.6(2)	90°	Sn2′	9.9(2)	90°
			Sn3′	4.9(2)	90°

Table 6.1: Hyperfine fields and angles (θ is the angle between V_{zz} and B_{hf}) for the Sn sites in the two states of $MnSn_2$, at similar temperatures (from ^{119}Sn Mössbauer spectroscopy). Results from Le Caër et al. [3].

tion of the magnetic structure are in direct response to a change in the anisotropic contribution. Therefore the anisotropic field at each Sn site and in each compound can be uniquely determined. In order to do so, a general expression for the hyperfine field transferred to the Sn sites must first be given.

In the ^{119}Sn study of the transferred hyperfine fields in $MnSn_2$, two distinct states were observed: state I ($90\text{ K} \leq T < 321\text{ K}$) in which there are two Sn sites with the area ratio ~50:50, and state II ($T \leq 70\text{ K}$) in which there are three Sn sites with the area ratio ~25:25:50. Table 6.1 summarizes the hyperfine fields and the θ angles for the Sn sites in the two states (recall from Chapter 2 that θ is the angle between the principal axis of the electric field gradient, V_{zz}, and the hyperfine field at the Sn site). All of the remaining Mössbauer parameters (quadrupole splitting, isomer shift, and linewidth) in the two states of $MnSn_2$ are the same within error. In the discussion of hyperfine fields in $MnSn_2$, Le Caër et al. [3] noticed two factors which were to have an impact on the final expression for B_{hf}, and they arose from comparing the observed and calculated θ and B_{hf}:

1. The θ angles for the possible orientations V_{zz} can be deduced by assuming that the Sn hyperfine field is collinear with the magnetic moment direction. These calculated angles however do not agree with those measured from Mössbauer (Table 6.2), so the hyperfine field must be partially or totally anisotropic (depending on the Sn site) [3].

Site	$V_{zz} \parallel X_1$	$V_{zz} \parallel X_2$	$V_{zz} \parallel X_3$
Sn1	90°	0°	90°
Sn2	0°	90°	90°
Sn1′	0°	0°	90°
Sn2′	0°	90°	90°
Sn3′	90°	90°	90°

Table 6.2: Calculated θ values if the Sn hyperfine field is parallel to the antiferromagnetic axis. The X_1, X_2 and X_3 axes are deduced from the four fold rotation [3].

2. The Sn lattice-dipolar fields due to the nearest Mn neighbours are two orders of magnitude less than the observed Mössbauer fields, thus making it necessary to consider that anisotropic fields exist that are due to the polarization of the $5p$ orbitals of Sn by covalency effects [3][49].

With the above factors in consideration, it was proposed that the transferred hyperfine field at the Sn sites be written as [3][4]:

$$\mathbf{B}_{hf} = \left(\mathrm{A}_p \sum_{i=1}^{6} \mathbf{u}_i(\vec{\mu}_i \cdot \mathbf{u}_i) - \frac{\mathrm{A}_p}{3} \sum_{i=1}^{6} \vec{\mu}_i \right) + \mathrm{A}_s \sum_{i=1}^{6} \vec{\mu}_i \tag{6.1}$$

where $\mathbf{u}_i$ is the unit vector connecting each Sn atom to a specific Mn atom with moment $\vec{\mu}_i$. A_p and A_s are the dipolar and contact fields due to a unit Mn moment. A_p is also referred to as the anisotropic constant.

The last term in equation 6.1 is the isotropic contribution from the Mn shells around the Sn atoms, while the first two terms represent the anisotropic part of the transferred hyperfine field. For the spin-reorientation and spin-flop, we will only consider the first term of equation 6.1:

$$\mathbf{A}_1 = \mathrm{A}_p \sum_{i=1}^{6} \mathbf{u}_i(\vec{\mu}_i \cdot \mathbf{u}_i) \tag{6.2}$$

because the second term is independent of moment direction. The dot product $(\vec{\mu}_i \cdot \mathbf{u}_i)$ is a maximum when the moment and Mn–Sn bond are parallel, and zero when they are perpendicular. From the crystal structure we know that the Mn–Sn bonds

Site	$\mathbf{A}_1/\mathrm{A}_p$		$\Delta\mathrm{A}_1/\mathrm{A}_p$
	$\vec{\mu} \parallel c$	$\vec{\mu} = (\frac{1}{\sqrt{2}}, \frac{1}{\sqrt{2}}, 0)\ \mu$	
Sn−2c	$(0, 0, 3.97\mu)$	$(0.72\mu, 0.72\mu, 0) \rightarrow 1.01\ \mu$	$2.96\ \mu$
Sn−2d	$(0, 0, 4.02\mu)$	$(0.70\mu, 0.70\mu, 0) \rightarrow 0.99\ \mu$	$3.03\ \mu$
Sn−2e	$(0, 0, 0.46\mu)$	$(1.96\mu, 1.96\mu, 0) \rightarrow 2.77\ \mu$	$-2.31\ \mu$

Table 6.3: Vector sum over the six Mn neighbours ($\mathbf{A}_1$) for the three Sn sites in $\mathrm{RMn_6Sn_6}$ for the Mn moments along the c−axis as well as in the ab−plane. The arrows in the third column indicate the magnitude $\mathrm{A}_1/\mathrm{A}_p$. Here, $\mu = \mu_{Mn}$.

make angles of 35° (Sn−2c and Sn−2d) and 73° (Sn−2e) with the c−axis. From the Mössbauer results discussed above (as well as magnetometry and neutron scattering [50]), we know that the moments point along c for $\mathrm{B}_o < \mathrm{B}_{sf}$ and in the ab−plane for $\mathrm{B}_o > \mathrm{B}_{sf}$. As all the angles and orientations are known for any B_o, the anisotropic constant A_p can be determined.

The values for $\mathbf{A}_1$ in any $\mathrm{RMn_6Sn_6}$ compound (as it is a consequence of the crystal structure and orientation of the Mn moments alone) at Sn−2c, Sn−2d and Sn−2e are listed in Table 6.3. As a preliminary example, we first discuss the anisotropic transferred fields in $\mathrm{TbMn_6Sn_{5.46}In_{0.54}}$, studied through the field-induced spin-flop at room temperature. When the applied field exceeds B_{sf}, the moments flop into the ab−plane from the c−axis. As a result, A_1 decreases at Sn−2c and Sn−2d, while it increases at Sn−2e. Comparisons between $\Delta\mathrm{A}_1/\mathrm{A}_p$ and $\Delta\mathrm{B}_{hf}$ show that despite the differences in their relative magnitudes, the signs agree for all three Sn sites. The sign of $\Delta\mathrm{A}_1/\mathrm{A}_p$ for each Sn site mirrors the behaviour of the overall transferred hyperfine fields of Figure 5.3 and Table 5.2, indicating that the anisotropic and isotropic contributions have the same sign.

In all of the compounds investigated here, the Sn−2e site was assigned by elimination: Sn−2c was assigned to the subspectrum which most reflected the values seen in $\mathrm{HfMn_6Sn_6}$, Sn−2d was assigned based on similarity to Sn−2c, while the remaining subspectrum was assigned Sn−2e. Here we see that Sn−2e is unique because it has a negative $\Delta A_1/A_p$ and ΔB_{hf}. This distinction allows the Sn$-2e$ site to be directly identified and confirms that the previous site assignment in the $RMn_6Sn_{6-x}X_x$ compounds (Chapters 3 through 5) were correct.

In the tetragonal $MnSn_2$ system ($I4/mcm$, $a = 6.659$ Å, $c = 5.447$ Å, with Mn$-4a$ at (0, 0, 0.25) and Sn$-8h$ at (0.1623, 0.6623, 0)), there is no spin reorientation or spin-flop, and ΔA_1 is simply A_1. The size of A_1/A_p is 0.96 μ_{Mn} and the magnitude of the Mn moment is $\mu_{Mn} = 2.33$ μ_B [51]. The antiferromagnetic environment of the Sn_{00} site guarantees that the transferred hyperfine field at Sn_{00} is purely anisotropic. The anisotropic transferred hyperfine field B^A_{hf} relates to the anisotropic constant A_p through:

$$A_p = \frac{B^A_{hf}}{\Delta A_1} \tag{6.3}$$

At Sn_{00}, $B^A_{hf} = 4.9(2)$ T [3], giving the anisotropic constant $A_p = 2.19(9)$ T/μ_B.

For the spin-flop in $TbMn_6Sn_{5.46}In_{0.54}$, the anisotropic field B^A_{hf} is taken as the difference between the $\mu \parallel c$ and $\mu \perp c$ hyperfine fields extrapolated to $B_o = 0$ T (δB_{hf} from Table 5.2). From room temperature studies of $TbMn_6Sn_6$, we know that the Mn moment is 1.99(6) μ_B [50]. The anisotropic constants from equation 6.3 are calculated as 0.03(3) T/μ_B, 0.40(2) T/μ_B and 0.89(3) T/μ_B for Sn$-2c$, Sn$-2d$ and Sn$-2e$ respectively. For the temperature-induced spin reorientation in $RMn_6Sn_{6-x}Ga_x$ (R = Tb, Er), the Mn magnetic moment must be considered at lower temperatures, because the anisotropic field is determined through an extrapolation to T_{sr} (in the spin-flop case, this extrapolation was to 0 T at room temperature, so the use of the 300 K value of the Mn moment in $TbMn_6Sn_6$ is valid).

A first concern is whether the Mn moment varies with Ga concentration. Table 6.4 gives the magnitude of the Mn moment for several compositions in $TbMn_6Sn_{6-x}Ga_x$ at 300 K, and shows that there is no large variation from compound to compound. Therefore, it is accurate enough for our purposes to use the value of the Mn moment in the ternary $TbMn_6Sn_6$ compound.

	$TbMn_6Sn_{6-x}Ga_x$		
T = 300 K	$x = 0$	$x = 0.2$	$x = 1.0$
μ_{Mn} (μ_B)	1.99(12)	1.98(8)	1.92(10)

Table 6.4: Mn magnetic moment values for several Ga concentrations in $TbMn_6Sn_{6-x}Ga_x$ at 300 K. Neutron scattering results from [12].

The thermal evolution of the magnetic moments is the now main concern. There have been many neutron diffraction studies of $TbMn_6Sn_6$, and the Mn moment is given for a few temperatures (335 K, 300 K, 250 K and 2 K) in [12]. The moment magnitude at these temperatures were fitted to a Brillouin function in order to determine the Mn moment at the different T_{sr} temperatures in $TbMn_6Sn_{6-x}Ga_x$. Table 6.5 lists the calculated Mn moments for the four Ga concentrations in $TbMn_6Sn_{6-x}Ga_x$.

x	T_{sr} (K)	μ_{Mn} (μ_B)
0.0	330	1.86
0.2	275	2.03
0.4	244	2.11
0.6	180	2.24
0.8	116	2.34

Table 6.5: Brillouin fit of the Mn magnetic moment with temperature, to give the magnitude at the various T_{sr} in $TbMn_6Sn_{6-x}Ga_x$.

At 2 K in $TbMn_6Sn_6$, $\mu_{Mn} = 2.39(8)\ \mu_B$ [50], and at 2 K in $ErMn_6Ge_{5.8}Ga_{0.2}$ (which should be near to that in $ErMn_6Sn_{5.89}Ga_{0.11}$), $\mu_{Mn} = 2.21(5)\ \mu_B$ [52]. Table 6.6 summarizes the anisotropic constants in three compounds for all three Sn sites, and Figure 6.1 gives the composition dependence of the anisotropic contribution in the $TbMn_6Sn_{6-x}Ga_x$ series. The anisotropic constants of the Sn−2*d* and Sn−2*e* sites in $TbMn_6Sn_{6-x}Ga_x$ seem to grow with increasing Ga content, indicating that larger Ga concentrations lead to greater anisotropic fields.

The anisotropic constants at the Sn sites in $RMn_6Sn_{6-x}X_x$ (R = Tb, Er; X = In, Ga) are significantly smaller than A_p measured at the Sn_{00} site in $MnSn_2$ (which is the

	A_p (T/μ_B)		
Site	$TbMn_6Sn_{5.46}In_{0.54}$	$TbMn_6Sn_{5.6}Ga_{0.4}$	$ErMn_6Sn_{5.89}Ga_{0.11}$
Sn−2*c*	0.03(3)	0.08(2)	0.14(6)
Sn−2*d*	0.40(2)	0.52(1)	0.58(4)
Sn−2*e*	0.89(2)	0.87(2)	0.90(4)

Table 6.6: Calculated anisotropic contributions to B_{hf} at the three Sn sites for different $RMn_6Sn_{6-x}X_x$ compounds.

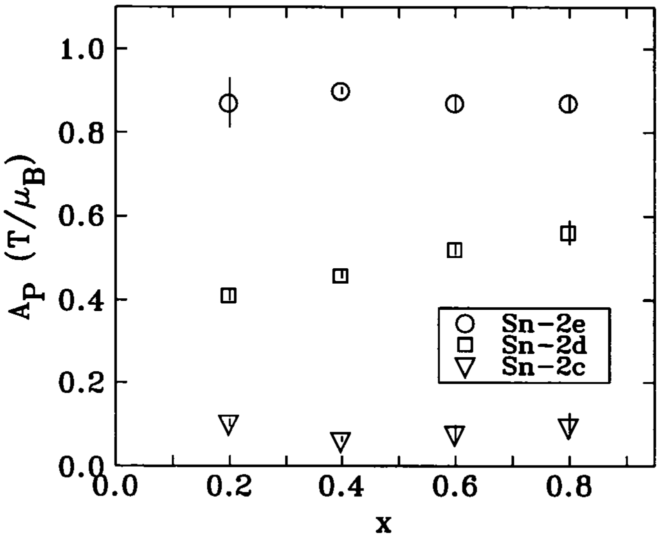

Figure 6.1: Anisotropic constants in all three Sn sites in $TbMn_6Sn_{6-x}Ga_x$ as a function of composition, x.

only site allowing for the cancelation of the isotropic contribution). As the anisotropic contribution is related to the localization of electrons on the Mn(Fe)–Sn bond, and therefore to covalency effects [3][4][53], the smaller anisotropic contributions seen here could indicate that the Mn–Sn bonds in the systems under investigation are less covalent. Parasitic anisotropic effects arising from Tb–Sn or Er–Sn bonding could also reduced the Mn–Sn anisotropic contribution (A_p) in this system.

Chapter 7

Conclusions

The Mössbauer study of the temperature-induced spin reorientation and the field-induced spin-flop (in (Er,Tb)$Mn_6Sn_{6-x}Ga_x$ and $TbMn_6Sn_{5.46}In_{0.54}$ respectively) has demonstrated that the anisotropic contribution to the transferred hyperfine field is independent of the force which drives the reorientation. We have used magnetometry and Mössbauer spectroscopy to show that the moments are along the $c-$axis for $T < T_{sr}$. The change in anisotropic field at the reorientation is seen to be largest at the Sn$-2e$ site, and the identification of this site is confirmed. The site preference for Ga substitution was shown to be Sn$-2d$, and there is slight evidence for substitution at Sn$-2e$. Finally, the anisotropic contribution to the transferred hyperfine field at the Sn sites in all of the compounds investigated was shown to be substantial, though less than in the $MnSn_2$ and $FeSn_2$ compounds. This is a possible consequence of weaker covalent bonding or contributions from Tb–Sn or Er–Sn bonds.

Future work

- The site preference obtained from the Mössbauer study of $RMn_6Sn_{6-x}Ga_x$ compounds differs from the neutron diffraction results. The $TbMn_6Sn_{6-x}In_x$ series should be investigated for comparison, because the In substitution in these compounds was shown to occur at the Sn$-2d$ site rather than Sn$-2c$.

- The investigation of the non-magnetic rare earth compounds $YMn_6Sn_{6-x}Ga_x$ should be performed with the intent of evaluating the possibility of a parasitic anisotropic effect from R–Sn (R = magnetic rare earth) bonding, which could reduce the Mn–Sn anisotropic contribution. The replacement of magnetic Tb with a non-magnetic rare earth atom also allows for further studies of covalency effects in the RMn_6Sn_6 system.

Bibliography

[1] T. Mazet, J. Tobola, G. Venturini, and B. Malaman, Phys. Rev. B **65**, 104406 (2002).

[2] G. Schatz and A. Weidinger, *Nuclear condensed matter physics: nuclear methods and applications* (Wiley, West Sussex, England, 1996), p. 126.

[3] G. Le Cäer, B. Malaman, G. Venturini, and I. Kim, Phys. Rev. B **26**, 5091 (1982).

[4] G. Le Caër, B. Malaman, G. Venturini, D. Fruchart, and B. Roques, J. Phys. F: Met. Phys. **15**, 1822 (1985).

[5] B. Malaman, G. Venturini, R. Welter, J.P. Sanchez, P. Vulliet, and E. Ressouche, J. Magn. Magn. Mater. **202**, 521 (1999).

[6] J.M. Cadogan and D.H. Ryan, J. Alloys and Compds **326**, 166 (2001).

[7] G. Venturini, B. Chafik El Idrissi, and B. Malaman, J. Magn. Magn. Mater. **94**, 35 (1991).

[8] J. Hu, K. Wang, and B. H. et al., J. Phys.: Condens. Matter **7**, 889 (1995).

[9] N.K. Zaikov, A.N. Pigorov, N.V. Mushnikov, A.E. Teplykh, É.Z. Valiev and Y. Dorofeev, JETP Letters **72**, 436 (2000).

[10] N. Spaldin, *Magnetic materials: fundamentals and device application* (Cambridge University Press, Cambridge, 2003), p. 76.

[11] J.M.D. Coey, *Rare-Earth Iron Permanent Magnets* (Oxford Science Publications, Dublin, 1996), p. 17.

[12] C. Lefèvre, G. Venturini, and B. Malaman, J. Alloys and Compds **358**, 30 (2003).

[13] D. Clatterbuck and K.A. Gschneidner Jr., J. Magn. Magn. Mater. **207**, 79 (1999).

[14] N. Spaldin, *Magnetic materials: fundamentals and device application* (Cambridge University Press, Cambridge, 2003), p. 124.

[15] B. Chafik El Idrissi, G. Venturini, and B. Malaman, Mater. Res. Bull. **26**, 432 (1991).

[16] Laura K. Perry, D.H. Ryan, G. Venturini and J.M. Cadogan, J. App. Phys. **99**, (April, 2006).

[17] F. Canepa, R. Duraj, C. Lefèvre, B. Malaman, A. Mar, T. Mazet, M. Napoletano, A. Szytula, J. Tobola, G. Venturini, and A. Vernière, J. Alloys and Compds **383**, 10 (2004).

[18] N. Spaldin, *Magnetic materials: fundamentals and device application* (Cambridge University Press, Cambridge, 2003), p. 107.

[19] C. Lefèvre and G. Venturini, J. Alloys and Compds **340**, 11 (2002).

[20] C. Lefèvre, G. Venturini, A. Vernière, and B. Malaman, J. Alloys and Compds **198**, 127 (1993).

[21] C. Lefèvre, G. Venturini, A. Vernière, and B. Malaman, J. Alloys and Compds **334**, 53 (2002).

[22] C. Lefèvre, G. Venturini, and B. Malaman, J. Alloys and Compds **329**, 76 (2001).

[23] C. Lefèvre, G. Venturini, and B. Malaman, J. Alloys and Compds **354**, 49 (2002).

[24] C. Lefèvre, G. Venturini, and B. Malaman, J. Alloys and Compds **346**, 84 (2002).

[25] L. Gelato, J. Appl. Cryst. **14**, 151 (1982).

[26] G. Venturini, private communications (2006).

[27] J.K. Srivastava, S.C. Bhargava, P.K. Iyengar and B.V. Thosar, *Advances in Mössbauer spectroscopy* (Elsevier Scientific Publishing Company, Amsterdam, 1983), p. 5.

[28] N.N. Greenwood and T.C. Gibb, *Mössbauer spectroscopy* (Chapman and Hall Ltd., Great Britain, 1971), p. 7.

[29] N.N. Greenwood and T.C. Gibb, *Mössbauer spectroscopy* (Chapman and Hall Ltd., Great Britain, 1971), p. 61.

[30] J.K. Srivastava, S.C. Bhargava, P.K. Iyengar and B.V. Thosar, *Advances in Mössbauer spectroscopy* (Elsevier Scientific Publishing Company, Amsterdam, 1983), p. 3.

[31] Christian J. Voyer, MSc. Thesis, McGill University (2005).

[32] G. Knoll, *Radiation detection and measurement* (John Wiley and Sons, USA, 1989), p. 230.

[33] N.N. Greenwood and T.C. Gibb, *Mössbauer spectroscopy* (Chapman and Hall Ltd., Great Britain, 1971), p. 9.

[34] N.N. Greenwood and T.C. Gibb, *Mössbauer spectroscopy* (Chapman and Hall Ltd., Great Britain, 1971), p. 10.

[35] N.N. Greenwood and T.C. Gibb, *Mössbauer spectroscopy* (Chapman and Hall Ltd., Great Britain, 1971), p. 46.

[36] N.N. Greenwood and T.C. Gibb, *Mössbauer spectroscopy* (Chapman and Hall Ltd., Great Britain, 1971), p. 374.

[37] N.N. Greenwood and T.C. Gibb, *Mössbauer spectroscopy* (Chapman and Hall Ltd., Great Britain, 1971), p. 55.

[38] J.K. Srivastava, S.C. Bhargava, P.K. Iyengar and B.V. Thosar, *Advances in Mössbauer spectroscopy* (Elsevier Scientific Publishing Company, Amsterdam, 1983), p. 18.

[39] J.M.D. Coey, *Rare-Earth Iron Permanent Magnets* (Oxford Science Publications, Dublin, 1996), p. 81.

[40] J.M.D. Coey, *Rare-Earth Iron Permanent Magnets* (Oxford Science Publications, Dublin, 1996), p. 84.

[41] N.N. Greenwood and T.C. Gibb, *Mössbauer spectroscopy* (Chapman and Hall Ltd., Great Britain, 1971), p. 90.

[42] Jin-lei Yao, Shao-ying Zhang, Juan Du, Mi Yan, De-ren Yang, Li-gang Zhang, Shi-min Liu, and Bao-gen Shen, Phys. Rev. B **67**, 134423 (2005).

[43] T. Mazet, M.N. Norlidah, B. Malaman, G. Venturini and R. Welter, unpublished (2005).

[44] N.N. Greenwood and T.C. Gibb, *Mössbauer spectroscopy* (Chapman and Hall Ltd., Great Britain, 1971), p. 417.

[45] C.G. Davies and J.D. Donaldson, J. Chem. Soc. (A), 946 (1968).

[46] G.S. Collins, T. Kachnowski, N. Benczer-Koller and M. Pasternak, Phys. Rev. B **19**, 1369 (1979).

[47] F. Canepa, M. Napoletano, R. Masini, C. Lefèvre, and G. Venturini, J. Phys.: Condens. Matter **in press**, (2005).

[48] C. Lefèvre, G. Venturini, and B. Malaman, J. Alloys and Compds **351**, 65 (2003).

[49] G. Venturini, unpublished (2005).

[50] J. Friedt, J. Sanchez, and G. Shenoy, J. Chem. Phys. **65**, 5093 (1976).

[51] B. Chafik El Idrissi, G. Venturini, B. Malaman, and D. Fruchart, J. Less Comm. Met. **175**, 143 (1991).

[52] L.M. Corliss and J.M. Hastings, J. App. Phys. **39**, 462 (1968).

[53] C. Lefèvre, G. Venturini, and B. Malaman, J. Alloys and Compds **335**, 26 (2002).

[54] G. Venturini and B. Malaman, Phys. Rev. B **35**, 7038 (1987).